Chapter 5
Nonlinear Structural Mechanics of Micro-and Nanosystems

Hassen M. Ouakad

In the nanoscale, when trying to fabricate straight clamped-clamped single-walled CNT transistors, the outcome comes as nonperfectly straight beam with an initial curvature, also called slack. Hence, we can see that understanding the dynamics of arches serve both the micro- and nanoworlds.

The dynamic behavior of CNTs also is greatly needed. Researchers have several reported unexplained and unjustified phenomena for electrically actuated slacked CNTs. These include multiple resonances, frequency crossing, frequency avoiding of crossing (veering), undistinguished resonances whether they are out-of-plane or in-plane, unexplained low values of quality factor, etc. A robust model of these complicated structures can reveal many of their dynamical related issues.

In the first part of this chapter, we summarize the main contributions in the area of modeling the structural mechanics of carbon nanotubes used as NEMS devices. We also address the need to add the slack effect when modeling CNTs. Then, we introduce general concepts (essentially reduced-order modeling and perturbation technique) in modeling the nonlinear structural mechanics problems of beams under several loading conditions (mainly electric actuation). We also include derivation of the equations of motion of MEMS arches along with discussing some conditions for applicability of the continuum theory in modeling the mechanical behavior of CNTs.

In the second part of this chapter, we present an investigation into modeling and analyzing the nonlinear structural mechanics of electrically actuated carbon nanotube resonators. We investigate in details the nonlinear structural mechanics of such devices including the effect of their initial curvature (level of slack). We present a framework and a platform to properly understand the dynamics of these complicated systems by explaining and revealing the meaning of their various detected resonance

H.M. Ouakad (✉)
Mechanical Engineering Department, King Fahd University of Petroleum and Minerals, Dhahran, Kingdom of Saudi Arabia
e-mail: houakad@kfupm.edu.sa

frequencies. Other topics that are covered include study of the possibility of energy exchange among the detected modes in slacked carbon nanotubes.

5.1 Literature Review

Since their discovery by Iijima [1] in 1991, CNTs attracted the interest of the nano scale world, especially the NEMS community [2, 3], due to their unique and distinguished mechanical and electrical properties. However, people how worked on investigating the dynamics of these tiny structures encountered serious obstacles such as their inherent nonlinear behavior even for very small dynamic loading [3], their low quality factors [4], detection of unexpected resonances, and unexplained patterns of the dependence of their natural frequencies on the gate voltage [5].

As an example for the structural related issues, it was shown that clamped-clamped CNT resonators are fabricated with some level of curvature (slack) when using the so-called Chemical Vapor Deposition (CVD) process [5]. This slack effect has shown to lead to various scenarios such as mode crossings, mode avoided crossings, multiple resonances, frequency crossing, frequency avoiding of crossing (veering), undistinguished resonances whether they are out-of-plane or in-plane, unexplained low values of quality factor, …etc [5, 6].

Estimating accurately the natural and resonant frequencies of CNTs has been the center of research attention over the past few years [7]. This is because predicting precisely the resonance frequencies forms the basis of utilizing CNTs as resonant sensors. In addition, relating the measured resonance frequencies to the predicted from theory has been proposed as an effective way to extract the mechanical properties of CNTs, such as Young's modulus [8, 9].

Clamped-clamped straight CNTs have been under extensive researches in the NEMS community. Most of the modeling work has especially focused on simulating their static response (linear and nonlinear) and free vibration (natural frequencies). Dequesnes et al. [10] used molecular dynamics and linear beam theory with electrostatic force to investigate pull-in and static behavior of CNT switches. The effect of van der Walls forces was studied and found negligible for gaps above 4 nm. Sapmaz et al. [11] investigated the static behavior and free vibrations of CNTs for various DC voltages using nonlinear beam equations for clamped-clamped beam assuming the DC load as constant. Dequesnes et al. [12] investigated pull-in and natural frequencies of clamped-clamped (including mid-plane stretching) and cantilever CNTs using molecular dynamics and continuum models. They concluded that nonlinear continuum model yields good match with molecular dynamics model.

Lefèvre et al. [13] measured the deflection versus DC for a clamped-clamped CNT using AFM to extract Young's modulus and simulated the static behavior of the CNTs using nonlinear beam theory. Ke and Espinosa [14] and Pugno et al. [15] conducted a nonlinear analysis for the static response of a doubly clamped CNT using a nonlinear elastic beam equation. Postma et al. [3] used a nonlinear model of clamped-clamped CNT along with a Galerkin procedure to descritize the beam

partial differential equation. They concluded that CNTs are almost useless in the linear regime even for small electric load and this due to the presence of thermal random noise. Witkamp et al. [16] and Poot et al. [17] presented modeling and testing of clamped-clamped CNTs. They used a beam model, including mid-plane stretching, to show the variations of natural frequencies of the CNT versus DC load. Peng et al. [18] used linear Euler–Bernoulli beam model to calculate the resonance frequency and quality factor.

Mecular dynamics (MD) analysis represented, in the past, the most used computational method in studying the physical as well as the mechanical behaviors of CNTs [12, 19–28]. In fact, MD can be accurately used to simulate the physical–chemical properties of CNTs at the atomic scale. But still being the most precise method in that fact, MD is of limited capabilities computationally point of view (maximum of 109 atoms [29] and 10–16 s as time step [30]. Basically in this method, the Newton's second law is applied for each considered atom forming the CNT (i.e., the acceleration term of each atom is equal to the spatial gradient of the empirical potential energy of the CNT). Then, the evaluation of that empirical potential energy is based on several methods such as: the force field method, the bond order method, and semiempirical method [31].

Several investigations have been conducted to simulate the response of CNTs using molecular dynamics and their results were compared to results obtained using continuum mechanics theories, such as beams and shells. All the investigations concluded that continuum mechanics serve the purpose of modeling and simulating CNTs both accurately and efficiently from a computational point of view. For example, Yakobson et al. [32] studied using a molecular dynamics model the large deformation of CNTs. They estimated the buckling of CNTs using continuum theory, a beam model, to the predictions of the molecular mechanics simulations. They concluded that this behavior of CNTs can be well described by a continuum model. Based on scaling analysis, Harik [33, 34] tackled the buckling problem of CNTs and proposed three nondimensional numbers related to the CNT geometric parameters to check the validity of the beam assumption for modeling the mechanics of CNTs. Liu and Chen [35] mentioned that investigating the global responses of CNTs such as deformations, effective stiffness, or load transfer can be done using continuum mechanics both effectively and efficiently. Pantano et al. [36] used finite element FE approaches to model a single-walled carbon nanotube SWCNT and a multi-walled carbon nanotube MWCNT. The CNT walls were modeled as thin shells while the inter-wall interactions were modeled as pressures. The pressures were defined as functions of separation distance. Pantano et al. [36] validated their model by comparing the FE results with the molecular mechanics simulations and the experimental data. They found good agreement among all the results. Arroyo and Belytschko [37] and Arroyo [38] also developed a FE model for MWNTs. They developed a membrane wall model directly using a Tersoff-Brenner potential and a modified Cauchy–Born rule. They were able to reproduce local buckling, kinking, and rippling effects, which are nearly identical to the deformed states of the parent molecular simulation, by using fine meshes for a variety of loadings including compression, torsion, and bending. They concluded that the continuum/finite element calculations are surpris-

ingly accurate compared to the atomistic calculations [38]. Dequesnes et al. [10, 12] employed a nonlinear beam theory in which they used the molecular dynamics simulations to extract the beam material properties (the beam bending (EI) and the beam stretching (EA) constants). They finally showed good agreement when comparing the beam model to the molecular dynamic simulations except for slight difference very close to pull-in. It was shown by Garg [31] that for the purpose of investigating the global behavior and response of CNTs, the continuum mechanics can be safely used under certain conditions.

In relatively more recent works, Wang et al. [39] remarked that atomistic and molecular methods are limited to CNTs with small number of atoms, due to the high cost of computation, and are therefore restrained to the study of localized effects on small portion of the CNT. In order to simulate the mechanical behavior of large-sized atomic CNTs, Wang et al. [39] proposed the use of continuum models. Sears and Batra [40] showed that continuum models predict both global and local responses for buckling of SWCNT by comparing their continuum predictions for bending and buckling to atomistic simulations. They employed a simple Euler beam to model the cantilever bending, and they ended up by showing that the continuum SWCNT strain energy was found to match that of the molecular simulation very well. Also, the buckling of a SWCNT was studied for tubes of different length to study and it was found to predict the critical buckling strain of the carbon nanotube for the whole length scale compared to molecular simulations.

Motivated by the 2-D problem of CNTs, Conley et al. [41] proposed a model for a CNT accounting for both the in- and out-of-plane motions. They reported the onset possibility of the non-planar motions in straight CNT resonators that they attributed to the symmetry of the device, as well as, to the nanotube stretching as it deforms.

Recently, Elishakoff and Pentaras [42] derived analytical expressions for the fundamental natural frequencies of double-walled carbon nanotubes under various boundary conditions (simply supported and doubly clamped) using two different decritization schemes, the Bubnov–Galerkin and the Petrov–Galerkin methods. They used a linear beam model and showed a possibility to quickly evaluate the natural frequencies of such systems. In another investigation [43], they adopted a simplified Bresse-Timoshenko beam model to evaluate the natural frequencies of simply supported CNTs taking into account the shear deformation as well as the rotary inertia effects. They showed that the model yields excellent results compared to the full Bresse-Timoshenko theory as well as the Euler–Bernoulli beam model. Lately, Georgantzinos et al. [44] proposed a linear spring-based model with lumped masses to describe and evaluate the vibration characteristics of a single-walled CNT. They observed that the aspect ratio has a significant role and influence on the basic modes of vibration of the nanotubes. Hawwa and Al-Qahtani [45] adopted an elastic continuum approach for modeling the primary resonance of a double-walled carbon nanotube under a linear harmonic excitation using the Galerkin approach. They showed several transitions from quasiperiodic to chaotic behavior accompanied with some nonlinear jump phenomena and nonlinear bifurcations leading to chaos.

Cantilever CNTs received less interest in modeling their nonlinear behavior. Among the few works on this field, Liu et al. [35] used a nonlinear beam model

(with cubic geometric nonlinearity) for a cantilever CNT. Ke and Espinosa [46, 47] presented the modeling of the static behavior of cantilever and doubly clamped CNTs. Ke et al. [48] studied theoretically and experimentally the static behavior of cantilever CNTs while considering the effect of the charge concentration, van der Wall forces, and the large kinematics (geometric nonlinearities). Isacsson et al. [49] investigated the dynamic response of a three-terminal cantilever CNT resonator structure. They used a perturbation theory to descritize the beam equation of motion and then determine analytically the frequency response of the system. Isacsson and Kinaret [50] modeled the parametric excitation of an array of cantilever CNTs excited by DC and AC excitations.

The above theoretical investigations were motivated especially by the several reported phenomenon of previously conducted experimental works [51–62].

Most of the previously mentioned literature work models clamped-clamped electrically actuated CNTs to be perfectly straight. However, due to their fabrication process using chemical vapor deposition (CVD), fabricating perfectly straight CNTs with controlled geometry and orientation is very difficult. Indeed, many studies have indicated that clamped-clamped CNTs are fabricated with some level of curvature (slack). Kang et al. [63] studied the interatomic interaction between a CNT bridge and the substrate underneath it used as a NEMS memory device. They showed that the value of the CNT bridge slack is very important for the operation of the NEMS memory device as a nonvolatile memory. Gibson et al. [7] stressed the importance of modeling the slack of CNTs and indicated that no consistent model has been presented so far to address this issue despite knowing the strong effect of the curvature of curved beams on modal frequencies.

Among those who reported experimental investigations showing the importance of slack on estimating accurately the natural frequencies of CNTs, Sazonova et al. [4] and Sazanova [5] tested slacked clamped-clamped CNT to a DC and AC load and characterized experimentally their free-vibration response. Comparing their experimental data with the numerical results of [6], they reported some unexplained phenomena [5]. Some of those experimentally observed phenomena are [5]: the sublinear variation of the frequencies, the avoided crossings (veering), the abundance of resonances, and the negative variation of the frequencies for certain carbon nanotubes. Üstünel et al. [6] were among the very few who attempted to investigate theoretically the effect of slack on a CNT oscillator. They based their work on a one-dimensional elastic continuum model by assuming the electrostatic force to be uniformly distributed along the length of the CNT and ignoring the nonlinear elastic effects. Then, they derived approximate analytical expressions of the natural frequencies of the CNT for several behavior regimes of the CNT depending on the gate voltage value. They identified three zones for the response: bending dominated, catenary dominated, and elastic dominated. They related this to the impact of slack on the natural frequencies. They reported that the bending regime can be described by a buckled doubly clamped beam model, the catenary regime is modeled as a simple string under variable tension, and the elastic regime is similar to the hanging chain under constant tension. Another group [64] attempted to model the CNT using a finite element method. They also reported discrepancy among their theoretically predicted and experimen-

tally measured resonance frequencies of electrostatically actuated CNTs and cited slack as a possible reason of this. Mayoof and Hawwa [65] proposed a nonlinear curved beam model to describe the nonlinear dynamics of a slacked single-walled carbon nanotube under linear harmonic excitation. They showed several scenarios of chaotic behavior for the CNT.

5.2 Background

In this section, we introduce general concepts in modeling the nonlinear structural mechanics problems of beams and then the case where electrostatic forces are used as actuation method. We also include derivation of the frequency equation using the so-called method-of-multiples scales. Finally, we present some conditions for applicability of the continuum theory in modeling the mechanical behavior of CNTs.

5.2.1 Beams

Beams are perhaps the most commonly used structural component in the MEMS and NEMS field. Micro and nanobeams form the backbone of a wide range of devices including resonators, resonant sensors, actuators, filters, atomic force microscope probes, and RF switches. They are also used as spring elements with other microstructures and MEMS components, such as comb-drive actuators.

(a) Equation of motion

Here, the linear equation of motion of a beam in bending is derived, The derivation here follows Hamilton's principle, which is variational mechanics energy-based approach. This presents an alternative technique to the Newtonian or vectorial method used in the derivations [66, 67]. Hamilton's principle is considered very powerful for deriving the equation of motion, along with the associated boundary conditions, of complicated distributed-parameter systems of multiple bodies and complicated boundary conditions. As an example, we will derive the equation of motion and associated boundary conditions governing the motion of an initially curved beam (arch beam) using the Hamilton's principle.

We consider a clamped-clamped shallow arch, Fig. 5.1, of initial shape $w_0(x)$, width b, thickness h, length L, modulus of elasticity E, cross sectional is $A = bh$, moment of inertia I, mass density ρ, and subjected to a constant axial force of magnitude N, as shown in Fig. 5.2. The axial displacement is denoted by $u(x, t)$ and the transverse displacement is denoted by $w(x, t)$ measured from the initial curvature $w_0(x)$. The beam is modeled according to the Euler–Bernoulli beam theory and in which the planes of the cross sections remain planes after deformation.

Fig. 5.1 Schematic of a clamped-clamped arch beam under a compressive axial load
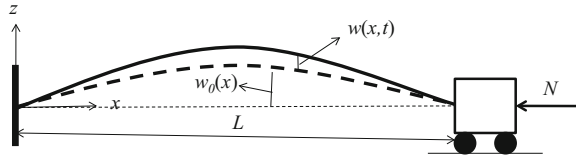
Fig. 5.2 Segment of the beam after deformation
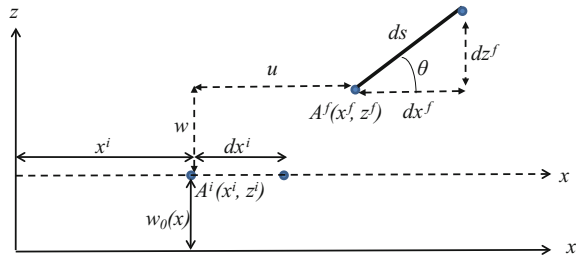
(i) The total axial strain

We first determine the geometrical relations of the beam points using Fig. 5.2. Figure 5.2 describes how a point A^i, with coordinates x^i and z^i in the axial and transverse directions respectively, moves to a point A^f with coordinates denoted by x^f and z^f after a deformation.

The geometrical relations are determined from Fig. 5.2 which contains a differential element located at the point A^i with length dx^i. The coordinates of A^f and the element length of the deformed configuration are determined respectively as follows, where the "'" denotes the derivative with respect to x:

$$\begin{cases} x^f = x^i + u = x + u, \\ z^f = z^i + w = w_0 + w, \end{cases} \tag{5.1}$$

$$ds = \sqrt{\left(dx^f\right)^2 + \left(dz^f\right)^2} = \sqrt{(dx + du)^2 + (dw + dw_0)^2}$$
$$= \sqrt{(1 + u')^2 + \left(w' + w_0'\right)^2}dx, \tag{5.2}$$

Now, under the assumptions of a shallow arch theory (the shallow arch approximation), in which the slope of the initial rise of the curved beam is considered smaller compared to unity [68], i.e., $\left(w_0'\right)^2 << 1$, Eq. (2.2) reduces to

$$ds = \sqrt{1 + 2u' + u'^2 + w'^2 + 2w'w_0'}dx \tag{5.3}$$

From the deformed element length, Eq. (2.3), we determine the strain of the deformed element and the stretch ratio for a small deformation, respectively, as

$$\varepsilon = \frac{ds - dx}{dx} = \sqrt{1 + 2u' + u'^2 + w'^2 + 2w'w_0'} - 1, \tag{5.4}$$

$$\lambda = \frac{ds}{dx} = \sqrt{1 + 2u' + u'^2 + w'^2 + 2w'w_0'} \tag{5.5}$$

The rotation angle, shown in Fig. 5.2, is determined as

$$\begin{cases} \sin(\theta) = \dfrac{dy^1}{ds} = \dfrac{w_0' + w'}{\lambda}, \\ \cos(\theta) = \dfrac{dx^1}{ds} = \dfrac{1 + u'}{\lambda}, \end{cases} \tag{5.6}$$

Differentiating Eq. (2.6), and using the shallow arch approximation, we get

$$\theta' = \frac{(1 + u')(w_0'' + w'') - u''(w_0' + w')}{\lambda^2} \tag{5.7}$$

The curvature of the arch mid-plane is given by

$$\begin{aligned} \kappa = \frac{d\theta}{ds} = \theta' \frac{dx}{ds} &= \frac{(1 + u')(w_0'' + w'') - u''(w_0' + w')}{\lambda^{3/2}} \\ &= \frac{(1 + u')(w_0'' + w'') - u''(w_0' + w')}{\left(1 + 2u' + u'^2 + w'^2 + 2w'w_0'\right)^{3/2}} \end{aligned} \tag{5.8}$$

Expanding Eqs. (2.4) and (2.8) up to the quadratic terms using a Taylor series expansion for small u' and w', we get

$$\varepsilon \approx u' + \frac{w'^2}{2} + w'w_0' + \cdots \tag{5.9}$$

$$\kappa \approx (w_0'' + w'') - u''(w_0' + w') - 2(w_0'' + w'')u' + \cdots \tag{5.10}$$

Now, the total axial strain at a point of distance z from the arch mid-plane line is measured to be

$$\varepsilon_T \approx \varepsilon - zw'' + \cdots \tag{5.11}$$

(ii) The kinetic and potential energies

Next, we develop expressions for the kinetic and potential energies of the arch beam. The potential energy due to the beam elastic deformation and the stretching of its mid-plane is given by

$$
\begin{aligned}
V &= \frac{1}{2} \int_0^l \int_{-h/2}^{h/2} \int_{-b/2}^{b/2} \left(E\varepsilon_T^2 \right) dydzdx, \\
&= \frac{E}{2} \int_0^l \int_{-h/2}^{h/2} \int_{-b/2}^{b/2} \left\{ \left(u' + \frac{w'^2}{2} + w'w_0' \right)^2 - zw'' \left(u' + \frac{w'^2}{2} + w'w_0' \right) + z^2 w''^2 \right\} dydzdx, \\
&= \frac{EA}{2} \int_0^l \left(u' + \frac{w'^2}{2} + w'w_0' \right)^2 dx + \frac{EI}{2} \int_0^l w''^2 dx,
\end{aligned}
$$

$$(5.12)$$

where $I = bh^3/12$.

The kinetic energy of the arch while neglecting the axial inertia term is given by

$$
T = \frac{\rho A}{2} \int_0^L \dot{w}^2 dx, \tag{5.13}
$$

where the dot denotes the partial derivative with respect to the time variable t.

(iii) The extended Hamilton principle

The Hamilton's principle is an important variational method in deriving the equation of motion and the associated boundary conditions of continuous systems. In such systems, the state is described by using continuous functions of space and time. The extended Hamilton Principle for such bodies is given by

$$
\int_{t_1}^{t_2} \delta L\, dt = \int_{t_1}^{t_2} \left(\delta T - \delta V + \delta W_e \right) dt = 0, \tag{5.14}
$$

where L is the Lagrangian, T is the kinetic energy, V is the elastic energy, W_e is the nonconservative work done by external loads on the system, and t_1, t_2 are the initial and final times, respectively.

The variation of the potential energy is obtained by integrating by parts over time Eq. (5.12) as follows:

$$
\begin{aligned}
&\int_{t_1}^{t_2} \delta V\, dt = \\
&\int_{t_1}^{t_2} \left\{ \begin{aligned}
& EA \left[\left(u' + \frac{w'^2}{2} + w'w_0' \right) \delta u \right]_0^L - EA \int_0^L \left(u' + \frac{w'^2}{2} + w'w_0' \right)' \delta u\, dx + \\
& + EA \left[\left(u' + \frac{w'^2}{2} + w'w_0' \right) w' \delta w \right]_0^L - EA \int_0^L \left(\left(u' + \frac{w'^2}{2} + w'w_0' \right) w' \right)' \delta w\, dx + \\
& + EA \left[\left(u' + \frac{w'^2}{2} + w'w_0' \right) w_0' \delta w \right]_0^L - EA \int_0^L \left(\left(u' + \frac{w'^2}{2} + w'w_0' \right) w_0' \right)' \delta w\, dx + \\
& + EI \left[w'' \delta w' \right]_0^L - EI \left[w''' \delta w \right]_0^L + EI \int_0^L w'''' \delta w\, dx
\end{aligned} \right\} dt
\end{aligned}
$$

$$(5.15)$$

The variation of the kinetic energy is obtained by integrating by parts over time Eq. (5.13) as follows:

$$\int_{t_1}^{t_2} \delta T \; dt = \frac{\rho A}{2} \int_{t_1}^{t_2} \delta \left[\int_0^L \left(\frac{\partial w}{\partial t} \right)^2 dx \right] dt = \rho A \int_0^L \int_{t_1}^{t_2} \left[\frac{\partial w}{\partial t} \left(\frac{\partial}{\partial t} \delta w \right) \right] dt \, dx,$$

$$= \rho A \left[\frac{\partial w}{\partial t} \delta w \right]_{t_1}^{t_2 \; t_1 = t_2} - \rho A \int_0^L \frac{\partial^2 w}{\partial t^2} \delta w \, dx = -\rho A \int_0^L \frac{\partial^2 w}{\partial t^2} \delta w \, dx,$$

$$\tag{5.16}$$

Finally, the variation of the nonconservative forces is given as follows:

$$\int_{t_1}^{t_2} \delta W_e \, dt = \int_{t_1}^{t_2} (F (x, t) \, \delta w - c \dot{w}) \, dt, \tag{5.17}$$

where F is a distributed load in the transverse direction and c is the viscous damping coefficient.

Plugging then Eqs. (5.15)–(5.17) into Eq. (5.14), and then collecting the terms with the arbitrary coefficient "δu", we get

$$\left(u' + \frac{w'^2}{2} + w' w_0' \right)' = 0 \tag{5.18}$$

Integrating Eq. (5.18) over the beam domain, we obtain the beam's axial elongation as

$$u (L, t) - u (0, t) = \left(u' + \frac{w'^2}{2} + w' w_0' \right) L - \int_0^L \left(\frac{w'^2}{2} + w' w_0' \right) dx, \tag{5.19}$$

where $u(L, t)$ and $u(0, t)$ are the axial displacements at the ends of the beam.

From Fig. 5.2, we have a fixed end at $x = 0$ and compressive axial load acting at the other end, hence

$$u (L, t) = -\frac{NL}{EA} \tag{5.20}$$

We finally obtain from Eqs. (5.18) and (5.20) that

$$u' + \frac{w'^2}{2} + w' w_0' = -\frac{N}{EA} + \frac{1}{L} \int_0^L \left(\frac{w'^2}{2} + w' w_0' \right) dx \tag{5.21}$$

Plugging now Eqs. (5.15)–(5.17) into Eq. (5.14), and then collecting the terms with the arbitrary coefficient "δw", we get

$$\rho A\ddot{w} + EIw'''' + c\dot{w} = EA\left(u' + \frac{w'^2}{2} + w'w'_0\right)'\left(w' + w'_0\right) +$$
$$+ EA\left(u' + \frac{w'^2}{2} + w'w'_0\right)\left(w'' + w''_0\right) + F(x,t) \quad (5.22)$$

Plugging Eqs. (5.18)–(5.21) into Eq. (5.22), we get the nonlinear equation of motion of the shallow arch [69]

$$\rho A\ddot{w} + EIw'''' + c\dot{w} = \left(-N + \frac{EA}{2L}\int_0^L (w'^2 + 2w'w'_0)dx\right)(w'' + w''_0) + F(x,t),$$
$$(5.23)$$

(b) Reduced-order modeling

If the equation characterizing the behavior of a beam is nonlinear or if the beam has some irregular geometrical and material properties, closed-form solutions may not be accessible. In such cases, numerical methods (such as Rayleigh–Ritz method, finite element method, and the weighted-residual method) need to be utilized to simulate the behavior of the beam. However, the previously mentioned methods can be inconvenient or even computationally very expensive, especially for multi-physics, nonlinear, and time-dependent problems, such as those commonly encountered in MEMS and NEMS. Hence, we propose to discuss a powerful technique, the Galerkin method, which is computationally efficient, capable of handling any systems, and suits nonlinear beams problems. Beam equations of motion cab be discretized using the Galerkin technique to yield a reduced-order model (ROM) [70]. To derive a ROM from a distributed-parameter system, one can either work with the Lagrangian [71], or work with the partial differential equations, boundary conditions, and orthogonality conditions of the beam [72]. We decide here to present the latter approach. We consider a general system with an equation and boundary conditions expressed respectively as

$$M(w(x,t)) = f(x,t), \quad (5.24)$$

$$BC_1(w) = w_1, \quad BC_2(w) = w_2, \quad (5.25)$$

where $w(x,t)$ is the dependent variable in space x and time t, M is a differential operator in space and time, which can be linear or nonlinear, $f(x,t)$ is the forcing term, BC_1 and BC_2 are boundary operators and w_1 and w_2 are non-time-varying boundary conditions. In the Galerkin discretization technique, we seek an approximate solution

of the above system in the form of

$$w(x, t) = \phi_0(x) + \sum_{i=1}^{n} u_i(t)\phi_i(x), \tag{5.26}$$

where $\phi_0(x)$ is a space function that satisfies the nonzero boundary conditions (w_1 and w_2 different of zero). If the boundary conditions are homogeneous ($w_1 = w_2 = 0$) then $\phi_0(x) = 0$. The time-varying functions $u_i(t)$ are to be determined for the sake to get the solution $w(x, t)$. The functions $\phi_i(x)$ are space-varying trial functions that should satisfy the following conditions [73]

- The homogenous form of all the boundary conditions of the problem ($w_1 = w_2 = 0$)
- Differentiable as the order of the differential equation of the system.
- Form and belong to a complete set of linearly independent functions.

To proceed, Eq. (5.26) is substituted into Eq. (5.24) yielding the following equation

$$M\left[\phi_0(x) + \sum_{i}^{n} u_i(t)\phi_i(x)\right] = f(x, t) \tag{5.27}$$

Then, multiplying Eq. (5.27) by ϕ_j, and integrating the equation over the domain of the problem yields

$$\int_{\Gamma} \phi_j(x)\left\{M\left[\phi_0(x) + \sum_{i}^{n} u_i(t)\phi_i(x)\right]\right\}dx = \int_{\Gamma} \phi_j(x)f(x, t)\,dx, \tag{5.28}$$

Once evaluating the integrals of Eq. (5.38), we get n differential equations in time of the $u_i(t)$ functions, which can be integrated numerically using Runge–Kutta techniques. Then the results are substituted back into Eq. (5.26) to yield the total response of the beam. The number n of necessary modes to ensure convergence needs to be examined.

The reduction of a distributed-parameter system of infinite degree of freedom or a partial differential equation in space and time into a number of ordinary differential equations in time (a finite-degree-of-freedom-system) is considered significant advantage from a computational point of view. Indeed, this is one of the major benefits of using the Galerkin method over finite element approaches. Thus, the Galerkin method is considered a powerful technique to generate reduced-order models. It is worth to mention that for static problems ($f(x, t) = f(x)$), the Galerkin discretization yields to a system of algebraic equations of unknown constant coefficients, which can be solved using Newton's Raphson methods.
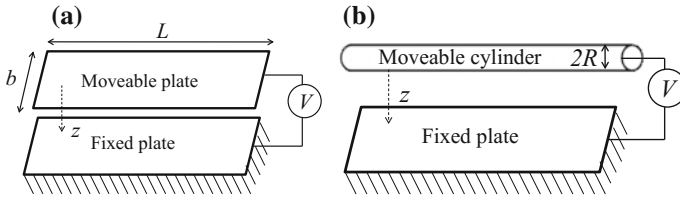
Fig. 5.3 Schematic of (**a**) a parallel-plates capacitor, and (**b**) a cylinder-plate capacitor

5.2.2 Electric Actuation

(a) About the actuation technique

Electrostatic loading is the most common actuation method in MEMS. The electrostatic actuation scheme is based on the simple parallel-plate capacitors. Those kinds of capacitors require a voltage source and they are characterized by having very low power consumption and being one of the fastest actuation methods. Electrostatic actuation depends on the attractive force between the two parallel plates of a capacitor, which is nonlinearly proportional to the gap width that separates both of them.

We will derive here the expression of the electrostatic force for two different cases: two parallel plates and two parallel cylinder and plate. We first consider the parallel-plate capacitor shown in Fig. 5.3. Here, we assume under the parallel-plate theory conditions that the electric field lines between the two considered plates are perpendicular to the plates even near edges (no fringing field effect near the edge of the plates).

Then, we assume that each capacitor shown in Fig. 5.3 is driven by a voltage source of load V. The electrical charge and the potential energy stored in each capacitor are given by the following expressions [74], respectively,

$$Q = C(z) V, \qquad (5.29)$$

$$E = \frac{V^2}{2} C(z) \qquad (5.30)$$

The attractive electrostatic force between each of the two electrodes of both the capacitors in Fig. 5.3 can be obtained as [74]

$$F_e = \frac{-\partial E(z)}{\partial z} = \frac{V^2}{2} \frac{\partial C(z)}{\partial z} \qquad (5.31)$$

Now, we will derive the analytical expressions of $C(z)$ depending on the geometries of the considered electrodes.

Considering the case of a capacitor formed by two parallel rectangular plates, Fig. 5.3a, the capacitance can be expressed as [74]

$$C(z) = \frac{\varepsilon_o L b}{z}, \tag{5.32}$$

where $\varepsilon_o = 8.85 \times 10^{-12} \left(C^2/Nm^2\right)$ is the air permittivity. We substitute Eq. (5.23) into Eq. (5.31) and get the attractive electrostatic force between the two electrodes of Fig. 5.3a

$$F_e = \frac{-\varepsilon_o b L V^2}{2z^2} \tag{5.33}$$

Now, we consider the case of a capacitor formed by parallel cylinder and rectangular plate, Fig. 5.3b. The capacitance can be expressed as [74]

$$C(z) = \frac{2\pi\varepsilon_o L}{\cosh^{-1}(1 + z/R)} \tag{5.34}$$

Substituting Eq. (5.34) into Eq. (5.31), we get the attractive electrostatic force between the two electrodes of Fig. 5.3b

$$F_e = \frac{-\pi\varepsilon_o L V^2}{\sqrt{z(z + 2R)} \left(\cosh^{-1}(1 + z/R)\right)^2} \tag{5.35}$$

We can notice, from both Eqs. (5.33) and (5.35), the inherent nonlinear dependence of the electrostatic force on the moveable electrodes (the planar electrode in Fig. 5.3a and the cylindrical electrode in Fig. 5.3b) displacement.

(b) The pull-in instability

In "parallel-plate" electrostatic actuation, Fig. 5.4a, a DC electrostatic load (V_{DC}) is applied between the lower and upper electrode, which is typically a flexible structure, such as a rectangular micro or nanobeam or a carbon nanotube. If V_{DC} is small, the structure stays in the deflected position, at which the elastic restoring force of the structure is in equilibrium with the opposing electrostatic force. There is an upper limit for V_{DC}, beyond which the mechanical restoring force of the structure can no longer resist the opposing electrostatic force. This leads to a sudden collapse of the structure, which is known as the pull-in instability [75–77]. Typically, the DC load tends to soften the actuated structure, which decreases its linear natural frequency [78].
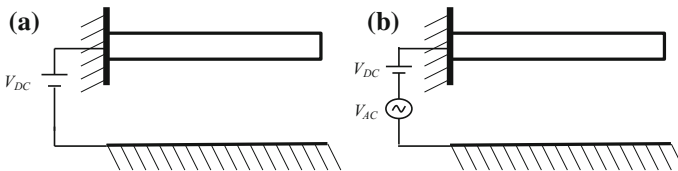
Fig. 5.4 Schematic of a parallel-plate electrostatic actuation with (**a**) DC load only, and (**b**) DC and AC harmonic load

Fig. 5.5 The pull-in band
(escape phenomenon) of an
electrically actuated system
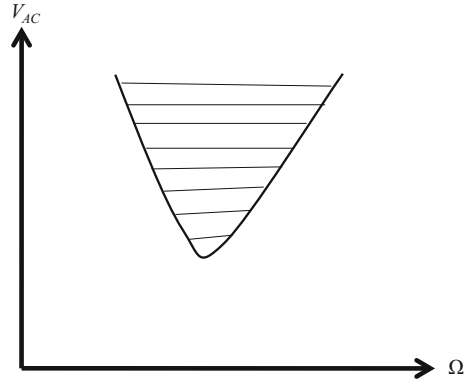
In addition to the DC electrostatic load of amplitude V_{DC}, resonant sensors and resonators are actuated by an AC harmonic load of amplitude V_{AC}, Fig. 5.4b. Here, V_{DC} deflects the movable electrode slightly and V_{AC} vibrates the electrode around the new deflected position. If V_{AC} is smaller than the dynamic pull-in limit and the structure is inherently nonlinear, such as the case of doubly clamped beams, then it can exhibit either softening or hardening behavior (depending on whether the electrostatic nonlinearity of quadratic nature dominates the geometric nonlinearity of cubic nature or vice versa). This effect of V_{AC} leads to a further shift in the resonance frequency, also called nonlinear resonance frequency [79–81]. While attempting to exceed the noise level of some structures, such as the thermal noises in CNTs [3, 51, 54], the V_{AC} amplitude might be raised to be high enough to trigger a dynamic pull-in instability [80, 82–84]. This instability, which characterizes the instability of the structure due to dynamics considerations, is called "dynamic pull-in".

For a certain DC and AC loads, the upper electrode can oscillate in a stable state, and varying the forcing frequency can lead to the dynamic pull-in phenomenon also referred to an escape from a potential well. Figure 5.5 shows a schematic of the escape band of the electrically actuated system of Fig. 5.4ba. The figure shows that for any dynamic load V_{AC} with frequency Ω in the shaded area then the escape phenomenon occurs definitely (inevitable escape) and for a frequency Ω lying in the nonshaded line, the system can oscillate in a stable state or escape from the potential well depending on its initial conditions (fractal behavior) [85, 86].

5.2.3 Perturbation Series and the Method of Multiple Scales

In this section, we review the application of a perturbation technique, for instance the method of Multiple Scales (MMS) to study the nonlinear dynamic of nonlinear systems.

(a) Perturbation series

Consider the set of ε-dependent ordinary differential equations given by

$$x' = f(x, t, \varepsilon), \tag{5.36}$$

where ε is a small parameter and for $\varepsilon = 0$ these equations can be easily solved. Then, a common approach in finding an approximate solution to Eq. (5.36), for small ε, is to approximate $x(t)$ in the following form of a "perturbation series"

$$x = x_0(t) + \varepsilon x_1(t) + \varepsilon^2 x_2(t) + \cdots \tag{5.37}$$

Then Eq. (5.36) can be expanded in powers of ε

$$x_0' + \varepsilon x_1' + \varepsilon^2 x_2' + \cdots = f(x, t, 0) + \frac{df(x, t, 0)}{d\varepsilon}\varepsilon + \cdots$$

$$= f(x_0, t, 0) + \varepsilon \left(\frac{df(x_0, t, 0)}{d\varepsilon} + \frac{df(x_0, t, 0)}{dx}(x_0 + 2\varepsilon x_1 + \cdots) + \cdots \right) + \cdots \tag{5.38}$$

Thus, an infinite sequence of simpler problems by equating terms with like powers of ε can be obtained. For example, gathering the terms of order 0 (terms multiplying ε^0)

$$x_0' = f(x, t, 0) \tag{5.39}$$

Once the order 0 problem is solved, the solution for x_0 may be plugged into the order ε^1-equation

$$x_1' = \frac{df}{d\varepsilon}(x_0, t, 0) + \frac{df}{dx}(x_0, t, 0)x_1, \tag{5.40}$$

and, hypothetically, this process can be iterated to solve for x_n at all orders.

In general, proving that a perturbation series converges or that it is asymptotic is hard.

(b) Method of multiple scales

The perturbation series expansion is not guaranteed to work for all dynamical problems. The nonlinear Rayleigh and Van Der Pol oscillators are two classical examples in which such an expansion fails. This is due to the fact that lower-order solutions $x_1, x_2, \ldots$, may grow without bound and eventually become large enough to interact strongly with higher-order terms. When this happens, treating the dynamics at different orders separately no longer makes sense. Generally speaking, this kind of failure occurs when there are two or more important scales in the system. For example, when a sound wave with a short wavelength travels through a slowly spatially varying medium, the resulting wave form looks locally like a sine wave when zooming into the wavelength scale. But on the length scale over which the medium properties vary substantially, the wave may exhibit significant phase drift or amplitude changes.

Solutions of the Rayleigh and Van Der Pol equations also have multiple scales, in the sense that on the order of one wavelength the solutions have frequency $\omega \approx \omega_0$, but over time scales of order ε^{-2} (Van Der Pol and Rayleigh) the solutions will have a significant phase drift.

The idea of this method is to pretend that an ODE is a PDE for a minute, where x depends both on time and on "slow time"; i.e.,

$$x = x_0(t, T) + \varepsilon x_1(t, T) + \varepsilon^2 x_2(t, T) + \ldots, \tag{5.41}$$

where $T = \varepsilon t$.

We then derive that

$$\frac{d(.)}{dt} = \frac{\partial(.)}{\partial t} + \frac{dT}{dt}\frac{\partial(.)}{\partial T} = \frac{\partial(.)}{\partial t} + \varepsilon \frac{\partial(.)}{\partial T} \tag{5.42}$$

and

$$\frac{d^2(.)}{dt^2} = \frac{\partial^2(.)}{\partial t^2} + 2\varepsilon \frac{\partial^2(.)}{\partial t \partial T} + \varepsilon^2 \frac{\partial^2(.)}{\partial T^2} \tag{5.43}$$

We write the original perturbation expansion in a more reminiscent form

$$x = \tilde{x}_0(t) + \varepsilon \tilde{x}_1(t) + \varepsilon^2 \tilde{x}_2(t) + \cdots, \tag{5.44}$$

where

$$\tilde{x}_n(t) = x_n(t, T(t)) \tag{5.45}$$

We then plug these substitutions into our equation, and proceed to solve it iteratively as a perturbation series. However, now the first-order equation will be sufficient only to determine x_0's dependence on time t, and not its dependence on t. This will leaves us free at order ε to tune the T dependence of x_0 to prevent x_1 from growing without bound.

(b) Application of the method of multiple scales

We propose now to approximate the dynamic responses of the Van der Pol and the Rayleigh oscillators using the method of Multiple Scales.

(i) The Van der Pol oscillator

We consider the Van der Pol oscillator in the case of a primary resonance Excitation; $\gamma = O(\varepsilon), \quad \Omega = \omega_0 + O(\varepsilon)$

$$\frac{d^2x}{dt^2} - \varepsilon(1 - x^2)\frac{dx}{dt} + \omega_0^2 x = f(t), \text{ with: } \begin{cases} f(t) = \gamma\varepsilon\cos(\Omega t) \\ \Omega = \omega_0 + \varepsilon\sigma \end{cases} \tag{5.46}$$

We seek an approximate solution of Eq. (5.46) using the method of Multiple Scales. In general, we consider $x(t)$ to be a function of multiple (two in this case) independent time variables or scales. We express x in the form

$$x = x_0(T_0, T_1) + \varepsilon x_1(T_0, T_1), \tag{5.47}$$

where $T_0 = t$ is a fast scale and $T_1 = \varepsilon t$ is a slow scale characterizing the modulation in the amplitude and phase caused by the nonlinearity, damping and resonances. The time derivatives become

$$\frac{d}{dt} = \frac{\partial}{\partial t} + \frac{dT}{dt}\frac{\partial}{\partial T} = D_0 + \varepsilon D_1 \tag{5.48}$$

so that

$$\frac{d^2}{dt^2} = D_0^2 + 2\varepsilon D_0 D_1, \tag{5.49}$$

where $D_n^= \partial/\partial T_n$. Substituting Eqs. (5.47)–(5.49) into Eq. (5.46) and equating the coefficient of ε^0 and ε^1 on both sides, we obtain

$$D_0^2 x_0 + \omega_0^2 x_0 = 0, \tag{5.50}$$

$$D_0^2 x_1 + \omega_0^2 x_1 + D_0 x_0 - x_0^2 D_0 x_0 + 2D_0 D_1 x_0 = \gamma \cos(\Omega T_0) \tag{5.51}$$

The solution of Eq. (5.50) can be expressed as

$$x_0 = A(T_1)\exp(i\omega_0 T_0) + \bar{A}(T_1)\exp(-i\omega_0 T_0) \tag{5.52}$$

Therefore, Eq. (5.51) becomes

$$D_0^2 x_1 + \omega_0^2 x_1 = i\omega_0[-2A' + A^2\bar{A} - A + \gamma\exp(i\sigma T_1)]\exp(i\omega_0 T_0)+ \\ +i\omega_0 A^3\exp(3i\omega_0 T_0) + cc, \tag{5.53}$$

where "cc" denotes the complex conjugate of the preceding terms. The secular terms can be eliminated from the solution of x_1 if

$$-2A' + A^2\bar{A} - A + \gamma\exp(i\sigma T_1) = 0 \tag{5.54}$$

We let $A = a\exp(i\beta)/2$ in Eq. (5.54), where a and β are real functions of the slow times scale T_1, and separate real and imaginary parts, to obtain

$$a' = \frac{a}{2}(1 - \frac{1}{4}a^2) + \frac{\gamma}{2\omega_0}\sin(\lambda), \tag{5.55}$$

$$a\beta' = -\frac{\gamma}{2\omega_0}\cos(\lambda), \tag{5.56}$$

where a' and β' are derivatives of the slow time scale T_1 and

$$\lambda = \sigma T_1 - \beta, \quad \frac{d\lambda}{dT_1} = \sigma - \frac{d\beta}{dT_1} \tag{5.57}$$

Eliminating β from Eqs. (5.55) and (5.56) gives

$$a\lambda' = a\sigma + \frac{\gamma}{2\omega_0}\cos(\lambda) \tag{5.58}$$

Therefore, to the first-order of approximation, we obtain

$$x = a\cos(\Omega t - \lambda) + O(\varepsilon) \tag{5.59}$$

For steady-state motion, the time variation of the amplitude and phase of the response must vanish $a' = \lambda' = 0$. It follows from Eqs. (5.55) and (5.56) that

$$\frac{a}{2}(1 - \frac{a^2}{4}) = -\frac{\gamma}{2\omega_0}\sin(\lambda), \tag{5.60}$$

$$a\sigma = -\frac{\gamma}{2\omega_0}\cos(\lambda) \tag{5.61}$$

The steady-state solution of Eq. (5.58), obtained by squaring and adding Eqs. (5.60) and (5.61), yields the following frequency-response equation:

$$\rho(\omega_0 - \rho)^2 + 4\sigma^2\rho = \frac{\gamma^2}{4\omega_0}, \text{ where } \rho = \frac{a^2}{4} \tag{5.62}$$

The frequency-response curves, in terms of the amplitude $\rho = a^2/4$, appear in Fig. 5.6 for selected values of the forcing amplitude γ. As γ increases, the curves consist of two branches. The first branch runs close to the σ-axis and the second branch is a close curve which can be approximated by an ellipse having its center

Fig. 5.6 Frequency-response curves for primary resonances of the Van der Pol Oscillator for various forcing amplitudes of γ ($\omega_0 = 1$ rad/s)
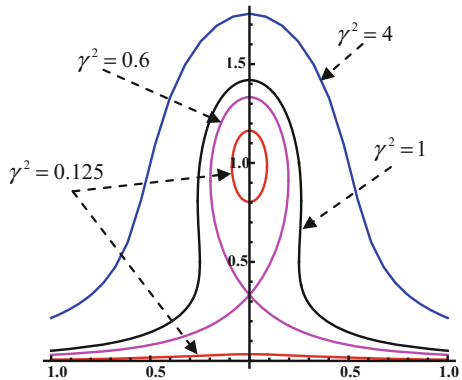
at the ρ-axis. As γ increases further, the ellipses expand; open and coalesce with the first branch to form a single branch of solutions and finally the response curves are single-valued for all σ. We note that in the $\sigma - \rho$ plane, the frequency-response curves, which are symmetric with respect to the σ axis, have shapes similar to those of the force-response curves.

When solving Eqs. (5.60) and (5.61), we can also obtain the first-order approximate solution in the following form:

$$x(t) = \sqrt{\frac{4\eta}{1 + (\frac{4\eta}{a_0^2} - 1)e^{-\varepsilon\eta t}}} \cos(\omega_0 t) + \frac{\gamma}{\omega_0^2 - \Omega^2} \cos(\Omega t), \text{ where: } \begin{cases} a_0 = x(0) - \dfrac{\gamma}{\omega_0^2 - \Omega^2} \\ \eta = 1 - \dfrac{\gamma^2}{2(\omega_0^2 - \Omega^2)^2} \end{cases}$$

$$(5.63)$$

Figure 5.7 shows that the approximate solution, for the Van der Pol oscillator using the perturbation technique, is close to that found using a numerical integration the oscillator's differential equation in Mathematica.

The second-order solution was derived using Mathematica [87] and Fig. 5.8 displays the resulting response.

Fig. 5.7 Comparison of the first-order approximate solution with the exact solution for the Van Der Pol oscillator for an initial condition of $x_0 = 0.01$, $\varepsilon = 0.1$. (In the figure: (——) the numerical solution, and the approximate solution using MMS(- - - - -))
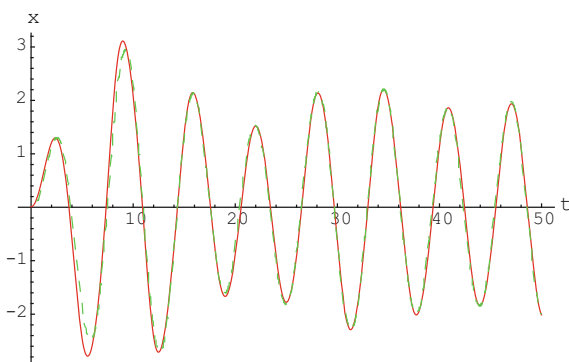
Fig. 5.8 Comparison of the second-order approximate solution with the exact solution for the Van Der Pol oscillator for an initial condition of $x_0 = 0.01$, $\varepsilon = 0.1$. (In the figure: (——) the numerical solution and the approximate solution using MMS(- - - - -))
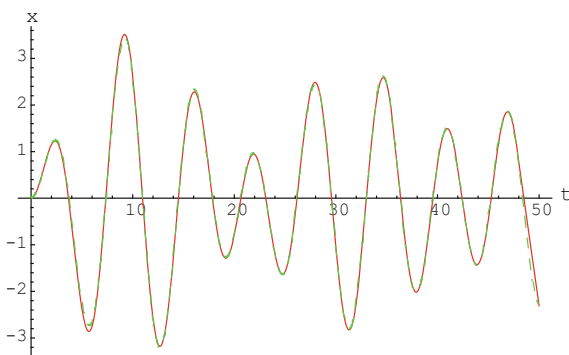
(ii) The Rayleigh oscillator

Now, let us consider the Rayleigh oscillator in the case of a primary resonance Excitation ($\gamma = O(\varepsilon)$, $\Omega = \omega_0 + O(\varepsilon)$). Its dynamics is described by the following equation:

$$\frac{d^2x}{dt^2} - \varepsilon\left(1 - \left(\frac{dx}{dt}\right)^2\right)\frac{dx}{dt} + \omega_0^2 x = f(t), \text{ with: } \begin{cases} f(t) = \gamma\varepsilon\cos(\Omega t) \\ \Omega = \omega_0 + \varepsilon\sigma \end{cases}, \quad (5.64)$$

We seek an approximate solution of Eq. (5.64) using the method of Multiple Scales. An approach similar to that followed in the van der Pol oscillator is used to determine the following frequency-response equation of this oscillator:

$$\varepsilon^2\rho(2\eta - \frac{3}{4}\rho)^2 + 4\sigma^2\rho = \gamma^2, \text{ where } \begin{cases} \rho = \omega_0^2 a^2 \\ \eta = 1/2 \end{cases} \quad (5.65)$$

Similarly, the approximate solution of Eq. (5.64) is expressed in the following form:

$$x(t) = \sqrt{\frac{8\eta\Big/3\omega_0^2}{1 + (\frac{8\eta}{3a_0^2\omega_0^2} - 1)e^{-2\varepsilon\eta t}}}\cos(\omega t) + \frac{\gamma}{\omega_0^2\Omega^2}\cos(\Omega t), \quad (5.66)$$

where

$$a_0 = x(0) - \frac{\gamma}{\omega_0^2 - \Omega^2}, \quad \eta = \frac{1}{2} - \frac{3}{4}\frac{\gamma^2\Omega^2}{(\omega_0^2 - \Omega^2)^2} \quad (5.67)$$

Figure 5.9 displays the approximate solution with the one obtained by numerically integrating Eq. (5.64). We can clearly see that the agreement is excellent among both approaches. Frequency-response curves generated from Eq. (5.65) are presented in Fig. 5.10.

Fig. 5.9 Comparison of the approximate solution with that obtained by integrating the original equation for an initial condition $x_0 = 0.01$, $\varepsilon = 0.1$. (In the figure: (——) the numerical solution and the approximate solution using MMS(-----))
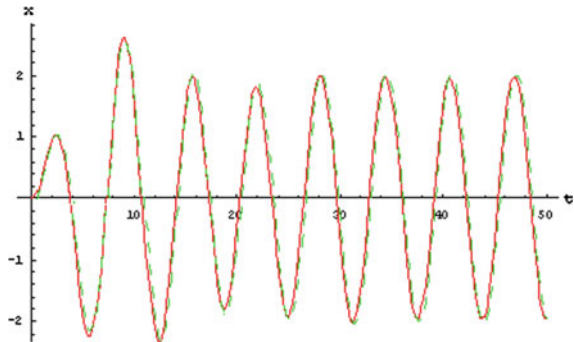
Fig. 5.10 Frequency-
response curves for primary
resonances of the Rayleigh
Oscillator for various forcing
amplitudes of
$\gamma (\omega_0 = 1 \, \text{rad/s, and } \varepsilon = 1)$

$\gamma^2 = 0.35$

$\gamma^2 = 0.2$

$\gamma^2 = 0.25$

$\gamma^2 = 0.1$
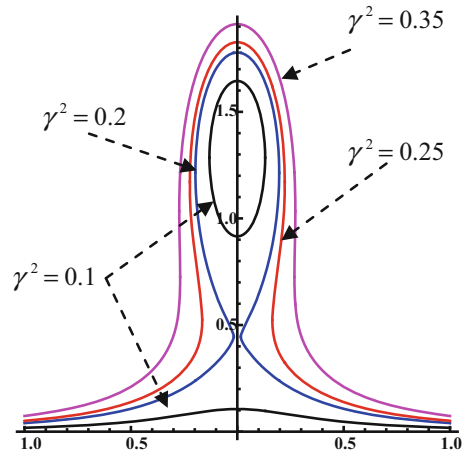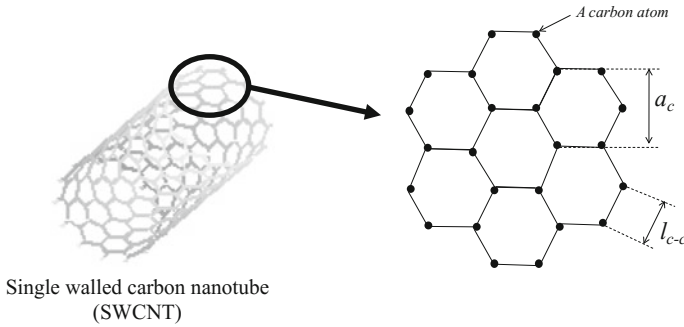
5.2.4 Carbon Nanotubes

(a) Structure overview

Single-walled carbon nanotubes (SWCNTs) can be considered to be formed by the rolling of a single layer of graphite (also called a graphene sheet) into a cylinder, Fig. 5.11.

Multi-walled carbon nanotubes (MWCNTs) can similarly be formed by considering coaxial assembly of cylinders of SWCNTs separated by the thickness of each graphene sheet.

Regarding the molecular structure of CNTs, they have a lattice-like structure [88] consisting of bounded carbon atoms, Fig. 5.11. Their geometric properties define their structural topology, which is likely similar to beams for small nanotube radius and to cylindrical shells for large nanotubes radius. This is true under certain specific conditions [34] that will be discussed later in this chapter. Figure 5.12 describes some of the geometric properties of CNTs, which are

Roll-up

Graphene sheet   Single walled carbon nanotube
                                                          (SWCNT)
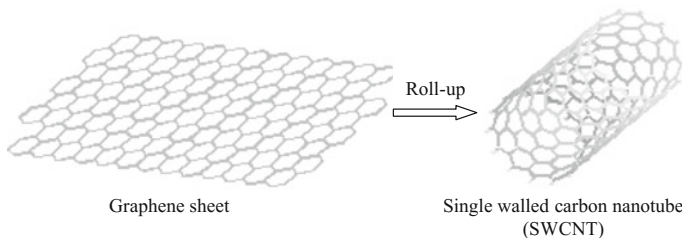
Fig. 5.11 Formation of a single-walled carbon nanotube from a graphene sheet

Single walled carbon nanotube
(SWCNT)

Fig. 5.12 Carbon atoms attachment in a single-walled carbon nanotube

- The distance of the adjacent carbon atoms (the length of the C–C bonds) denoted by l_{c-c} and found typically to be equal to 0.14 nm.
- The width of the hexagonal carbon rings denoted by a_c, which is typically equal to 0.24 nm [89].

Other important properties that define the geometry of a nanotube and that are not represented in Fig. 5.12 are

- The diameter of the nanotube (d_{NT}) which can be ranged from 0.4 nm to 100 nm and even higher [33, 34].
- The interlayer spacing (h) also called the graphene shell thickness found to be equal to 0.34 nm [33, 34]
- The length of the nanotube (L_{NT}) that may also range from 1 nm to 10 micrometer [33].

(b) The applicability of the continuum mechanics in modeling CNTs

In the following, we will present criteria for the applicability of the continuum mechanics in simulating the response of CNTs. Although some simulation results achieved in the literature were based on the molecular dynamics method, as we reviewed in Sect. 4.1, this method is still limited to CNTs with a small number of atoms and is therefore restrained to the study of small-scale modeling such as localized effects on small portions of the CNTs. So, in order to simulate the mechanical behavior of large-sized atomic CNTs, the continuum model was show to be practical in analyzing large-scale and the global mechanical behavior of CNTs [39] but under certain conditions [34].

Based on scaling analysis, Harik [33, 34] proposed following three nondimensional numbers to check the validity of the beam assumption for modeling the mechanics of CNTs:

- The homogenization criteria of the nanotube that ensures the molecular length-scales and described by the following equation:

$$a_c/L_{NT} \prec 1 \qquad (5.68)$$

- The aspect ratio criteria described by the following equation:

$$d_{NT}/L_{NT} \prec 1 \qquad (5.69)$$

- The linearity of strains criteria described by the following equation:

$$(L_{NT} - (L_{NT})_0)/L_{NT} \prec 1 \qquad (5.70)$$

As will be shown later on, we have verified that all the applicability conditions of the continuum theory as stated by [34] are satisfied for the CNTs under consideration in this work.

5.3 Structural Behavior of Straight Carbon Nanotube Resonators

In this section, we investigate the nonlinear static and dynamic of both cantilevered and clamped-clamped straight carbon nanotubes (CNTs). We present numerical approaches and methodologies to predict and simulate the dynamic behavior of CNTs when driven by AC and DC loads ranging from small to large values. We will present numerical approaches to calculate accurately the resonance frequency of clamped-clamped and cantilever CNTs accounting for the effects of their geometric nonlinearities, DC and AC loads. This in turn should lead to accurate calibration and prediction for the mechanical properties of CNTs by relating the measured nonlinear resonance frequencies to the predicted one based on a proper model. Then, we present in-depth investigation for the dynamic response of CNT resonators when driven by large values of AC and DC loads. Instability regimes of the resonators as a function of the frequency and amplitude of the AC load will be shown. The instability regimes can increase the knowledge about the limitations and practical applications of the CNTs when used as resonators.

5.3.1 Problem Formulation

Here, we formulate the problem for the static and dynamic behavior of an electrically actuated CNT resonator. The considered boundary conditions for the CNT are a
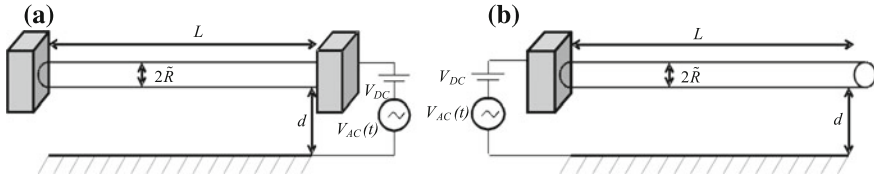
Fig. 5.13 Schematic of the electrically actuated (**a**) clamped-clamped and (**b**) cantilever CNT resonator

clamped-clamped beam, Fig. 5.13a, and a cantilever beam, Fig. 5.13b. The CNT is actuated by an electrode underneath it with a gap width d. It is modeled as an Euler-Bernoulli cylindrical beam of radius $\tilde{R}$, length L, and a quality factor Q. It has a cross-sectional area $A = \pi \tilde{R}^2$, area moment of inertia $I = \pi \tilde{R}^4/4$, natural frequency $\omega_n = \beta^2 \sqrt{EI/\rho AL^4}$ (β is equal to 4.73 for the case of a clamped-clamped beam and equal to 1.875 for the cantilever beam), and damping coefficient $\tilde{c} = \rho A \omega_n / Q$. The carbon nanotube is assumed to have a Young's modulus $E = 1\ TPa$ and a density $\rho = 1.35\ \mathrm{g/cm^3}$ [90].

The equation of motion of a clamped-clamped and cantilever carbon nanotube resonator, Fig. 5.13a, b, can be written as [10, 12]

$$EI \frac{\partial^4 w}{\partial x^4} + \rho A \frac{\partial^2 w}{\partial t^2} + \tilde{c} \frac{\partial w}{\partial t} = F_{non} + F_{elec}, \tag{5.71}$$

where ε_0 is the air permittivity and the geometric nonlinearity term F_{non} is written for clamped-clamped and cantilever CNTs, respectively as

$$F_{non}^{clamped} = \left(\frac{EA}{2L} \int_0^L \left(\frac{\partial w}{\partial x} \right)^2 dx \right) \frac{\partial^2 w}{\partial x^2}, \tag{5.72}$$

$$F_{non}^{can} = EI \frac{\partial}{\partial x} \left[\frac{\partial w}{\partial x} \frac{\partial}{\partial x} \left(\frac{\partial w}{\partial x} \frac{\partial^2 w}{\partial x^2} \right) \right] \tag{5.73}$$

The electrostatic force per unit length expression is given as follows (see background section, Eq. (5.35)

$$F_{elect} = \frac{\pi \varepsilon_0 (V_{DC} + V_{AC} \cos(\tilde{\Omega}))^2}{\sqrt{(d-w)(d-w+2\tilde{R})} \left(\cosh^{-1} \left(1 + \frac{d-w}{\tilde{R}} \right) \right)^2} \tag{5.74}$$

The boundary conditions for the clamped-clamped CNT are

$$w(0, t) = 0, \quad \frac{\partial w}{\partial x}(0, t) = 0, \quad w(L, t) = 0, \quad \frac{\partial w}{\partial x}(L, t) = 0, \tag{5.75}$$

and for the cantilever CNT

$$w(0, t) = 0, \quad \frac{\partial w}{\partial x}(0, t) = 0, \quad \frac{\partial^2 w}{\partial x^2}(L, t) = 0, \quad \frac{\partial^3 w}{\partial x^3}(L, t) = 0 \qquad (5.76)$$

For convenience, we introduce the following nondimensional variables:

$$\hat{w} = \frac{w}{d}, \qquad \hat{x} = \frac{x}{L}, \qquad \hat{t} = \frac{t}{T}, \qquad (5.77)$$

where T is a time constant defined by $T = \sqrt{\rho A L^4 / EI}$. Next, by dropping the hats, the nondimensional equations of motions and associated boundary conditions for the clamped-clamped and cantilever carbon nanotubes are written respectively as

$$\frac{\partial^4 w}{\partial x^4} + \frac{\partial^2 w}{\partial t^2} + c\frac{\partial w}{\partial t} = \alpha_1 \left(\int_0^1 \left(\frac{\partial w}{\partial x} \right)^2 dx \right) \frac{\partial^2 w}{\partial x^2} +$$
$$+ \frac{\alpha_2 (V_{DC} + V_{AC} \cos(\Omega t))^2}{\sqrt{(1 - w)(1 - w + 2R)} \left(\cosh^{-1} \left(1 + \frac{1 - w}{R} \right) \right)^2}, \qquad (5.78)$$

$$w(0, t) = 0, \quad \frac{\partial w}{\partial x}(0, t) = 0, \quad w(1, t) = 0, \quad \frac{\partial w}{\partial x}(1, t) = 0, \qquad (5.79)$$

$$\frac{\partial^4 w}{\partial x^4} + \frac{\partial^2 w}{\partial t^2} + c\frac{\partial w}{\partial t} = \alpha_3 \frac{\partial}{\partial x} \left[\frac{\partial w}{\partial x} \frac{\partial}{\partial w} \left(\frac{\partial w}{\partial x} \frac{\partial^2 w}{\partial x^2} \right) \right] +$$
$$+ \frac{\alpha_2 (V_{DC} + V_{AC} \cos(\Omega t))^2}{\sqrt{(1 - w)(1 - w + 2R)} \left(\cos h^{-1} \left(1 + \frac{1 - w}{R} \right) \right)^2}, \qquad (5.80)$$

$$w(0, t) = 0, \quad \frac{\partial w}{\partial x}(0, t) = 0, \quad \frac{\partial^2 w}{\partial x^2}(1, t) = 0, \quad \frac{\partial^3 w}{\partial x^3}(1, t) = 0, \qquad (5.81)$$

where

$$\alpha_1 = 2\left(\frac{d}{R}\right)^2, \quad \alpha_2 = \frac{\pi \varepsilon_0 L^4}{EI d^2}, \quad \alpha_3 = \left(\frac{d}{L}\right)^2, \quad c = \tilde{c}\frac{L^4}{EI}, \quad \Omega = \frac{\tilde{\Omega}}{\omega_n}, \quad R = \frac{\tilde{R}}{d} \tag{5.82}$$

The Reduced-Order Model

To simulate the response of the CNT, Eqs. (5.78)–(5.81) are discretized using the Galerkin procedure to yield a ROM. Hence, the deflection of the CNT is approximated as

$$w(x, t) = \sum_{i=1}^{n} u_i(t) \phi_i(x), \qquad (5.83)$$

where $\phi_i(x)$ are the normalized linear undamped mode shapes of a straight beam and $u_i(t)$ are the nondimensional modal coordinates. To obtain the ROM, we substitute Eq. (5.83) into Eqs. (5.78)–(5.81), multiply by $\phi_i(x)$, use the orthogonality conditions of the mode shapes, and then integrate the outcome from 0 to 1. The results are differential equations in terms of the modal coordinates $u_i(t)$.

Several points need to be clarified about the developed ROM. Unlike the case of MEMS [72], here there is no numerical advantage of multiplying Eq. (5.78) or Eq. (5.80) by the denominator of the electrostatic force term since the mode shape $\phi_i(x)$ will remain embedded inside the square root term and the inverse hyperbolic cosine term even after imposing the orthogonality of the mode shapes. To deal with the complicated integral terms due to the electrostatic force, we evaluated the spatial integrals containing the $\phi_i(x)$ terms numerically, using a trapezoidal method, simultaneously while integrating the differential equations of the modal coordinates $u_i(t)$ with time.

As an example, assuming one mode, the modal equation describing $u_1(t)$ for a clamped-clamped CNT is written as

$$\ddot{u}_1(t) + C\dot{u}_1(t) + Ku_1(t) = \alpha_1 \Gamma u_1^3(t) +$$
$$+ \int_0^1 \frac{\alpha_2(V_{DC} + V_{AC}\cos(\Omega t))^2 \phi_1(x)}{\sqrt{(1 - \phi_1(x)u_1(t))(1 - \phi_1(x)u_1(t) + 2R)}\left(\cosh^{-1}\left(1 + \frac{1 - \phi_1(x)u_1(t)}{R}\right)\right)^2} \, dx,$$
(5.84)

where

$$K = \int_0^1 \left(\phi_1(x)\phi_1^{iv}(x)\right)dx, \qquad C = c\int_0^1 (\phi_1(x))dx, \qquad (5.85)$$

and

$$\Gamma = \left[\int_0^1 \left(\phi_1(x)\phi_1''(x)\right)dx\right]\left[\int_0^1 \left(\phi_1'(x)\right)^2 dx\right] \qquad (5.86)$$

The Static Analysis

Various case studies of carbon nanotubes are considered for simulations, Table 5.1. We first examine the convergence of the ROM. Figure 5.14 shows the normalized maximum static deflection of a clamped-clamped carbon nanotube $w_{max} = w_s(x = 0.5)$ for case 2 of Table 5.1 using one, two, and three symmetric modes of the ROM while varying the DC load. It follows from the figure that using one mode yields acceptable converged results. This result shows a clear difference between CNTs and other MEMS beams [72], where at least three symmetric modes need to be used for convergence. One possible justification for this is due to the high stiffness of CNTs making the contribution of the higher-order modes weak compared to the first one.

Next, we verify the obtained results using one mode in the ROM by comparing them with the simulation results of Pugno et al. [15], which are based on a finite-difference method. Following Pugno et al. [15], we first conduct a comparison

Table 5.1 The geometrical properties of the studied carbon nanotube beams

Case #	Boundary conditions	d [nm]	L [nm]	$\tilde{R}$ [nm]	References
1	Clamped-clamped	100	3000	20	[15]
2	Clamped-clamped	100	3000	30	[15]
3	Clamped-clamped	100	2000	30	[15]
4	Cantilever	390	2500	5.45	[91]
5	Cantilever	3000	6800	23.5	[47]

Fig. 5.14 Variation of the normalized static deflection of the carbon nanotube with the DC voltage for case 2 of Table 5.1. In the figure: (○) one-mode ROM, (●) two modes ROM, and (*) three modes ROM
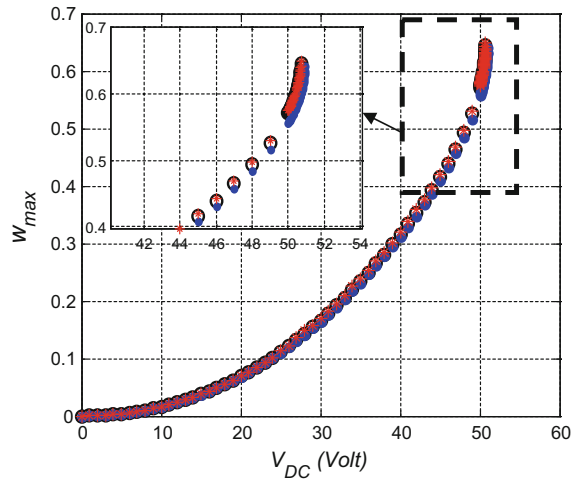
assuming a linear beam model for the case of clamped-clamped carbon nanotube (without mid-plane stretching). Figure 5.15a shows the results for cases 1 and 2 of Table 5.1 indicating excellent agreement between our results and the results of Pugno et al. [15]. In addition, we show the unstable branches of the equilibrium solutions. We can see that both the unstable and stable branches collide at pull-in. Also, it is worth to note that pull-in occurs here at a normalized deflection approximately equal 0.46, compared to 0.33 in the linear case of electrostatically actuated structures [78]. This can be attributed to the geometrical shape of the carbon nanotube and the difference between the electrostatic force field in this case and the case of parallel-plate rectangular shaped capacitor.

Next, we include the mid-plane stretching term in the simulation and compare with the nonlinear model results of Pugno et al. [15], Fig. 5.15a. The figure also shows excellent agreement; thereby validating the ROM. Comparing Fig. 5.3a, b, one can see the importance of mid-plane stretching in predicting accurately the pull-in voltage of the carbon nanotube. Further, it is noted that pull-in occurs here at $w_{max} = 0.64$, compared to 0.45 in the nonlinear case of an electrostatically actuated microbeam of rectangular cross section [72]. Table 5.2 shows a comparison between
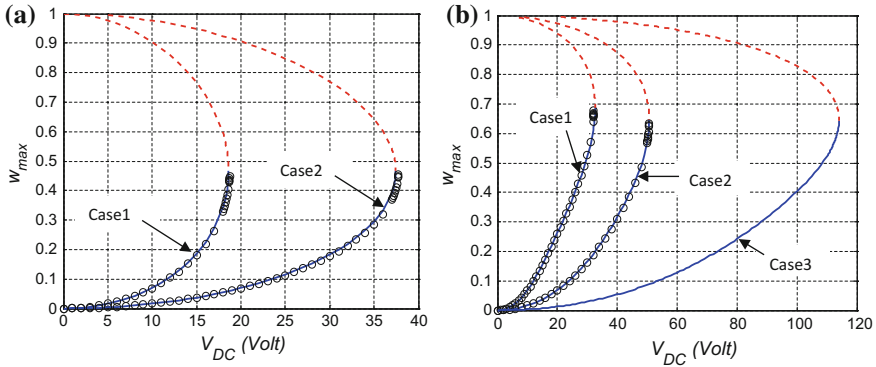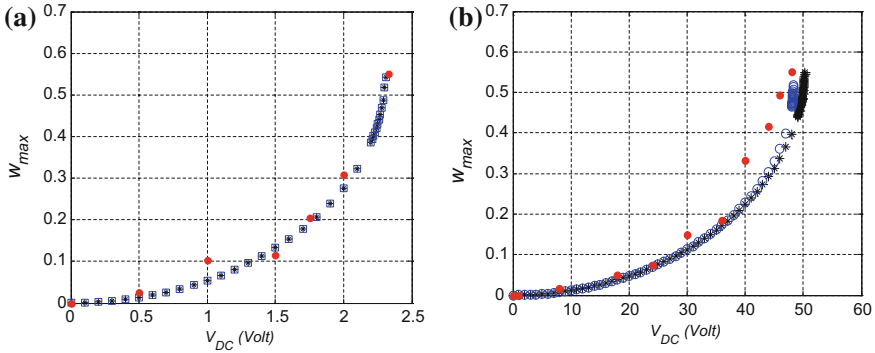
Fig. 5.15 Variation of the normalized static deflection of clamped-clamped carbon nanotubes with the DC voltage, (**a**) without including mid-plane stretching and (**b**) with including mid-plane stretching. In the figure: (—-) stable branch, (-----) unstable branch, and (○) results of Pugno et al. [15]

Table 5.2 The calculated pull-in voltages for the cases of Table 5.1

Case #	Pull-in voltage [Volt] (linear theory)	Pull-in voltage [Volt] (nonlinear theory)
1	18.62	32.65
2	37.46	50.72
3	82.47	114.2
4	2.309	2.31
5	50.20	48.26

the calculated pull-in voltage for the cases of Table 5.1 using linear and nonlinear beam theories. As noted from the table, the error in using linear theory to predict the behavior of CNTs can be significant.

Next, we show results for cantilever carbon nanotubes. In Fig. 5.16a, b, we validate the one-mode ROM results for the cantilever CNT case by comparing them with the experimental data reported in Akita et al. [91] and Pugno et al. [15]. In the figures, the normalized maximum static deflection of the cantilever carbon nanotube is $w_{max} = w_s(x = 1)$. The ROM includes the geometric nonlinearities of the cantilever CNT. In Fig. 5.16a, b, the parameters of cases 4 and 5 of Table 5.1 were used, respectively. The experimentally measured pull-in voltages are 2.33 Volt [91] and 48.26 Volt [15] for cases 4 and 5, respectively, whereas the obtained values using the ROM are 2.31 Volt and 48.26 Volt. It is clear that the experimental data and the ROM results are in good agreement. As noted, the effect of the geometric nonlinearities in the cantilever case is less than it is for the case of clamped-clamped carbon nanotubes.

Fig. 5.16 Variation of the normalized static deflection of cantilever carbon nanotubes with the DC voltage for (**a**) Case 4 of Table 5.1 and (**b**) Case 5 of Table 5.1. In the figure: (*) ROM (one mode, linear case), (□) ROM (two modes, linear case), (○) ROM (two modes, nonlinear case), and (●) experimental data of (**a**) Akita et al. [91] and (**b**) Pugno et al. [15]

Free-Vibration Problem Under a DC Voltage

(a) Numerical approaches

In this section, we present two computationally-efficient approaches to solve the free-vibration problem of the CNT under a DC electrostatic load. First, we use the ROM of Sect. 4.3.2. In this approach, the static deflection of the CNT needs to be solved for each DC voltage. For a given voltage, we substitute the stable static solution, found by solving the static equations as we did in Sect. 4.3.3, into the Jacobian matrix of the ROM. Then, the eigenvalues of the calculated Jacobian matrix are solved. By taking the magnitudes of each individual eigenvalue, the natural frequencies of the system are obtained. This is similar to what we have been done in [92, 93].

The second approach that can be used is through solving numerically the original boundary value problem, Eq. (5.71), using numerical software such as Mathematica® [87]. This approach is considered more accurate compared to the ROM since the latter approximates the original problem while the former deals with the problem exactly. This approach can be applied on Eqs. (5.71) and (5.72) for clamped-clamped CNTs combined with a shooting technique to iterate on the integral term of Eq. (5.72) [78]. Also, it can be applied directly on Eqs. (5.71) and (5.73) for cantilever CNTs. However this technique suffers convergence problems for clamped-clamped CNTs because of the mid-plane stretching term. To resolve this problem, one can split the in-plane equation from the out-of-plane equation in Eq. (5.71) and then solve the coupled system. Here, out-of-plane means motion transversal to the beam axis (toward the substrate) and in-plane means across the beam length. Next, we rewrite the beam equation as two coupled partial differential equations governing the transverse, w, and axial, u, deflections of the beam as [94, 95].

$$EI\frac{\partial^4 w}{\partial x^4} + \rho A\frac{\partial^2 w}{\partial t^2} = EA\left(\frac{\partial u}{\partial x} + \frac{1}{2}\left(\frac{\partial w}{\partial x}\right)^2\right)^2\frac{\partial^2 w}{\partial x^2} +$$
$$+ \frac{\pi\varepsilon_0(V_{DC} + V_{AC}\cos(\tilde{\Omega}t))^2}{\sqrt{(d-w)(d-w+2\tilde{R})}\left(\cosh^{-1}\left(1+\frac{d-w}{\tilde{R}}\right)\right)^2}, \tag{5.87}$$

$$\rho A\frac{\partial^2 u}{\partial t^2} = EA\left(\frac{\partial^2 u}{\partial x^2} + \frac{\partial w}{\partial x}\frac{\partial^2 w}{\partial x^2}\right) \tag{5.88}$$

The boundary conditions governing w and u respectively are

$$w(0,t) = 0, \quad \frac{\partial w}{\partial x}(0,t) = 0, \quad w(L,t) = 0, \quad \frac{\partial w}{\partial x}(L,t) = 0,$$
$$u(0,t) = 0, \quad u(L,t) = 0 \tag{5.89}$$

Because the natural frequency in the axial direction is much larger than the one in the transverse direction [95], we drop the inertia term of the u component in Eq. (5.88), and get the following equation:

$$\frac{\partial^2 u}{\partial x^2} = -\frac{\partial w}{\partial x}\frac{\partial^2 w}{\partial x^2} \tag{5.90}$$

Equations (5.87) and (5.90) can now be solved simultaneously for u and w. Using the nondimensional variables defined in Eq. (5.77) and dropping the hats yield

$$\frac{\partial^4 w}{\partial x^4} + \frac{\partial^2 w}{\partial t^2} = \alpha_1\left(\frac{\partial w}{\partial x}\right)^2\frac{\partial^2 w}{\partial x^2} + \alpha_4\frac{\partial u}{\partial x}\frac{\partial^2 w}{\partial x^2} +$$
$$+ \frac{\partial_2(V_{DC} + V_{AC}\cos(\Omega t))^2}{\sqrt{(1-w)(1-w+2R)}\left(\cosh^{-1}\left(1+\frac{1-w}{R}\right)\right)^2}, \tag{5.91}$$

$$\frac{\partial^2 u}{\partial x^2} = -\alpha_3\frac{\partial w}{\partial x}\frac{\partial^2 w}{\partial x^2}, \tag{5.92}$$

where α_1, α_2, α_3 are given by Eq. (5.82) and $\alpha_4 = 4(L/\tilde{R})^2$.

We split the transverse and axial deflections into static components due to the DC voltage, denoted by $w_s(x)$ and $u_s(x)$ respectively, and dynamic components denoted by $w_d(x,t)$ and $u_d(x,t)$ respectively, that is,

$$w(x,t) = w_s(x) + w_d(x,t), \tag{5.93}$$

$$u(x,t) = u_s(x) + u_d(x,t) \tag{5.94}$$

Substituting Eqs. (5.93) and (5.94) into Eqs. (5.91) and (5.92), dropping the AC forcing term, and retaining only the linear terms in w_d and u_d yields the following equations describing the small free vibration of the clamped-clamped carbon nanotube:

$$w_d'''' + \ddot{w}_d = \alpha_1(w_s'^2 w_d'' + 2w_s' w_s'' w_d^1) + \alpha_4(u_s' w_d'' + w_s'' u_d^1) +$$

$$+ \left(\frac{\alpha_2 V_{DC}^2 \left(2\sqrt{(1-w_s)(1-w_s+2R)} + (1-w_s+R)\cosh^{-1}\left(1 + \frac{1-w_s}{R}\right) \right)}{((1-w_s(1-w_s)(1-w_s+2R))^{\frac{3}{2}} \left(\cosh^{-1}\left(1 + \frac{1-w_s}{R}\right) \right)^3} \right) w_d, \quad (5.95)$$

$$u_d'' = -\alpha_3 w_s' w_d'' - \alpha_3 w_s'' w_d' \qquad (5.96)$$

To derive the eigenvalue problem, we let

$$w_d(x,t) = \Phi(x) e^{i\omega t}, \qquad (5.97)$$

$$u_d(x,t) = \psi(x) e^{i\omega t}, \qquad (5.98)$$

where $\Phi(x)$ and $\psi(x)$ are the associated transverse and axial eigenfunctions respectively and ω is the nondimensional natural frequency. Substituting Eqs. (5.97) and (5.98) into Eqs. (5.95) and (5.96) and solving the resulting equations yield the mode shapes Φ and ψ and their associated natural frequency ω.

(b) Results

To start, we use a one mode approximation in the ROM of Sect. 4.3.2 to calculate the natural frequencies and then compare the results to those obtained by solving the boundary value problem directly. In Fig. 5.17, we compare the variation of the first natural frequency of a clamped-clamped CNT (case 2 of Table 5.1) using the two methods. We can conclude from the figure that the one-mode ROM converges and follow the CNT behavior even near the pull-in instability.

Figure 5.18a depicts the fundamental natural frequency calculated using the ROM (o) and the results of Dequesnes et al. [12] for a clamped-clamped carbon nanotube of length = 20.7 nm, radius = 0.9 nm, and gap width = 3 nm. The figure shows that the natural frequency decreases slightly for small ranges of the DC voltage, then increases again as the effect of mid-plane stretching of the CNT increases, and then drops suddenly to zero near pull-in. As seen in the figure, the model shows high robustness in tracking the increase and then the drop of the natural frequency to zero near pull-in. Also, the figure indicates good agreement with the results of Dequesnes et al. [12], which were obtained by a molecular dynamics model.

Because the gap width of this case study is too small (below 3 nm), van der Walls forces can have significant effect on the results [12]. To investigate this effect, we add the van der Walls forces term to the beam equation, which becomes [10, 12]
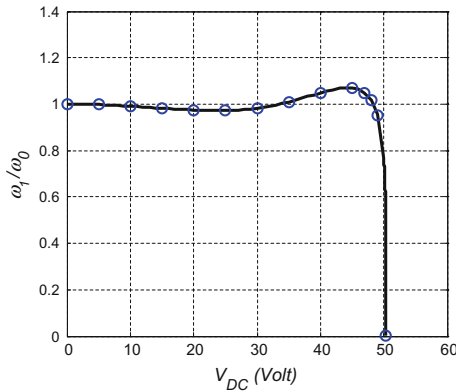
Fig. 5.17 Variation of the fundamental natural frequency ω_0 normalized with that at zero voltage ω_0 for various values of DC voltage. Results are shown for the carbon nanotube of case 2 of Table 5.1. In the figure: (○) are the results obtained by solving the boundary value problem directly and (—-) are those obtained using a one-mode ROM

$$EI\frac{\partial^4 w}{\partial x^4} + \partial A\frac{\partial^2 w}{\partial t^2} + \tilde{c}\frac{\partial w}{\partial t} = \left(\frac{EA}{2L}\int_0^L \left(\frac{\partial w}{\partial x}\right)^2 dx\right)\frac{\partial^2 w}{\partial x^2} + F_{elec} + F_{vdw},$$

(5.99)

where

$$F_{elect} = \frac{\pi\varepsilon_0(V_{DC} + V_{AC}\cos(\tilde{\Omega}t))^2}{\sqrt{r(r+2\tilde{R})}\left(\cosh^{-1}\left(1+\frac{r}{\tilde{R}}\right)\right)^2},$$

$$F_{vdw} = -\frac{C_6\pi^2\sigma^2\tilde{R}\sqrt{r(r+2\tilde{R})}(8r^4 + 32r^3\tilde{R} + 72r^2\tilde{R}^2 + 80r\tilde{R}^3 + 35\tilde{R}^4)}{2r^5(r+2\tilde{R})^5},$$

(5.100)

where $r = d - w$ is the distance between the CNT and the substrate, $C_6 = 15.2eV \overset{o}{A}$ is a constant characterizing the interaction between two carbon atoms and $\sigma = 38\,\text{nm}^{-2}$ is the substrate layer (graphite) surface density. By applying the procedure of Sects. 4.3.2 and 4.3.4 on Eqs. (5.99) and (5.100), we obtain the natural frequencies under the effect of both the electrostatic and van der Walls forces.

Figure 5.18a compares the obtained results with and without the van der Walls forces. As seen, in this case the van der Walls forces have negligible effect. Figure 5.18b shows another case of smaller gap width, $d = 1\,\text{nm}$, for a clamped-clamped carbon nanotube of length $= 20.7\,\text{nm}$ and radius $= 0.9\,\text{nm}$. The figure shows comparisons among the results of the ROM and Dequesnes et al. [12] with and without van der Walls forces. There are good agreements among all results. In this case, as shown from Fig. 5.18b, the van der Walls forces have significant impact on changing the natural frequencies and the pull-in voltage. It is worth to mention that
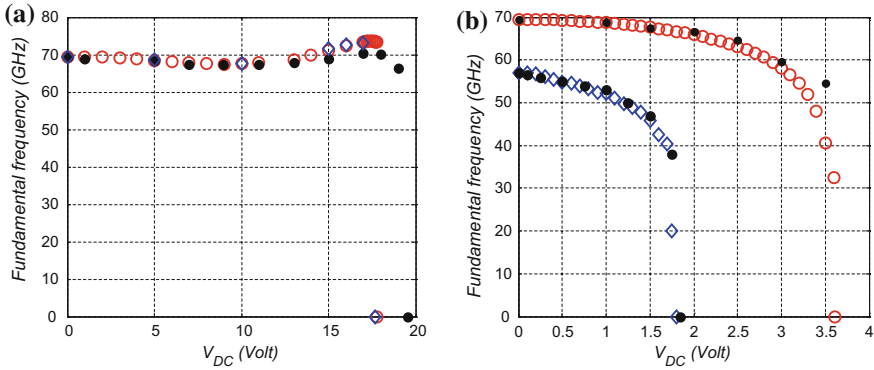
Fig. 5.18 Variation of the fundamental natural frequency with the DC voltage for two clamped-clamped carbon nanotubes. Figure 5.18a is for a CNT of length 20.7 nm and gap width 3 nm and Fig. 5.18b is for a CNT of length 20.7 nm and gap width 1 nm. In the figure: (∘) ROM without including van der Wall forces, (◇) ROM with including van der Wall forces, and (●) results of Desquesnes et al. [12]

Fig. 5.19 Variation of the normalized fundamental natural frequency ω_1 with the DC voltage for clamped-clamped carbon nanotubes for case 1 (∘), case 2 (*), and case 3 (●) of Table 5.1
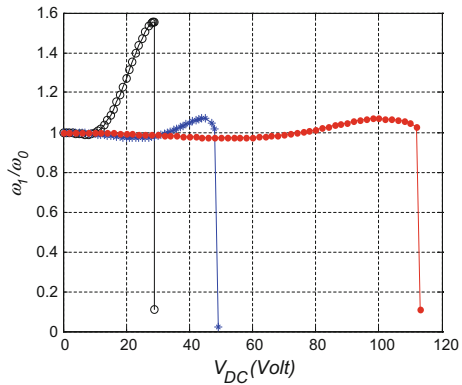
from a computational point of view, the ROM is very cheap compared the molecular dynamics model of Dequesnes et al. [12].

Figure 5.19 shows the variation of the fundamental natural frequency of the clamped-clamped CNTs for cases 1, 2, and 3 of Table 5.1. As seen in the figure, the fundamental frequency increases to higher values as the electrostatic force increases for all the considered cases and then decreases to zero when pull-in occurs. This is due to the fact that the effect of mid-plane stretching dominates that of the electrostatic force. This agrees with the reported experimental data of [4]. One can see from Fig. 5.19 that both parameters (the length and the radius) of the CNT can be used to tune the fundamental natural frequency to be almost unchanged over an extended range of DC voltages (see the curve of case 3). This attractive feature can be promising for the implementation of CNTs as resonant sensors.

Fig. 5.20 Variation of the fundamental natural frequency with the DC voltage for a cantilever carbon nanotube (case 4 of Table 5.1)
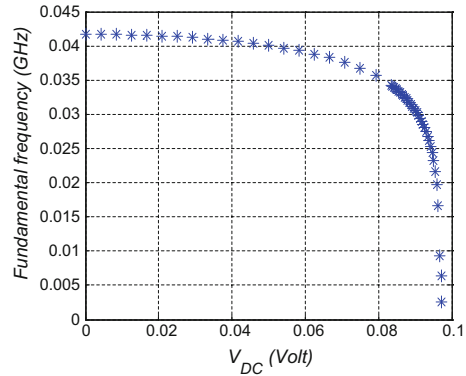

We end this section by showing the variation of the natural frequency of a cantilever CNT with the DC voltage. Because of the fact that the geometric nonlinearity is weak in this case, the electrostatic force is always dominant and hence the CNT experiences a softening behavior. Figure 5.20 shows simulation results for the cantilever beam of case 4 of Table 5.1. We notice in the figure a monotonic decrease in the natural frequency until it reaches zero at pull-in.

Dynamic Response to DC and AC Loads

(a) Primary resonance of the fundamental mode

Here, we simulate the frequency-response of the carbon nanotube when excited by a DC load superimposed to an AC harmonic load of frequency near its fundamental natural frequency (primary-resonance excitation, $\Omega \approx \omega_1$). In the dynamic analysis, long-time integration for the reduced-order model equations of motion can be used. However, this method suffers convergence problems near bifurcations and instabilities and in general is not considered a robust method for studying nonlinear vibrations. Hence, a second method will be used, which is called the shooting technique [96]. The shooting method is a numerical technique to find periodic solutions, analyze their stability, and also locate and identify bifurcation points. This method will be used in conjunction with the Floquet theory [96] to study the stability of the captured periodic orbits.

We first investigate the response of carbon nanotubes to small AC and DC load (Figs. 5.21 and 5.22). In all subsequent figures, dashed lines refer to unstable solutions. Figure 5.21 shows a frequency-response curve of a clamped-clamped CNT of case 2 of Table 5.1. The figure compares the results of the shooting technique, based on one mode approximation, to the long-time integration technique using one and two modes in the ROM. The figure verifies the convergence of the ROM for the dynamic simulations and the fact that one mode yields adequate accuracy. Figure 5.9 shows a hardening behavior of the clamped-clamped CNT even for this small value of electric load, which is away from the pull-in voltage (50.7 Volt). This represents another sign for the dominant effect of mid-plane stretching of clamped-clamped
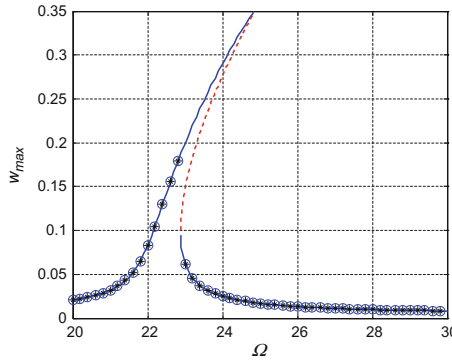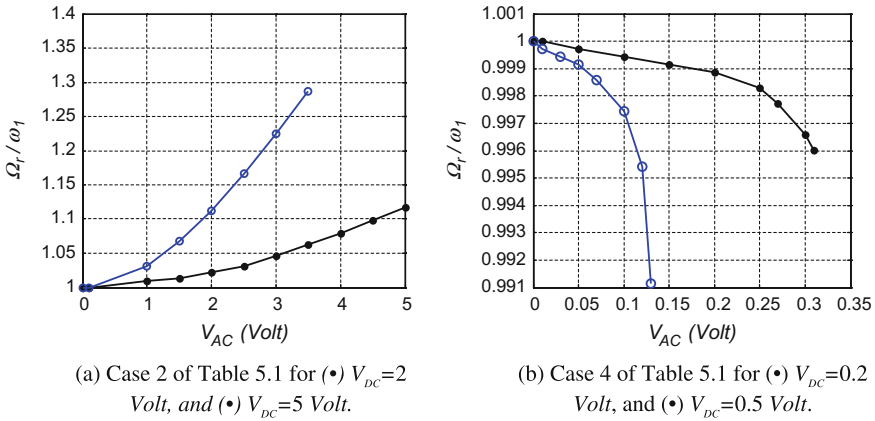
Fig. 5.21 Frequency-response curve of the CNT for case 2 of Table 5.1 shows the shift in the non-linear resonance frequency in the hardening-behavior case. Results are shown for $V_{DC} = 5$ Volt, $V_{AC} = 2$ Volt, and Q = 100. In the figure, $w_{max} = w(0.5, t)$ is the mid-point/maximum deflection of a clamped-clamped CNT, (——) shooting method (stable branch), (- - - -) shooting method (unstable branch), (*) long-time integration (one-mode ROM), and (◦) long-time integration (two modes ROM)
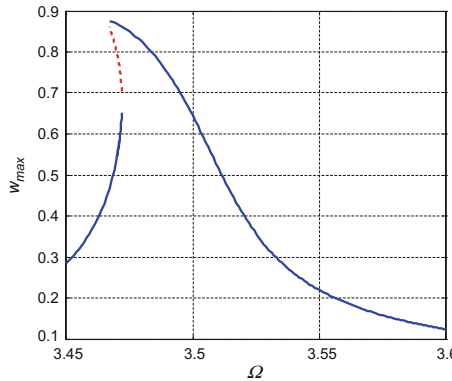
Fig. 5.22 Frequency-response curve of the CNT for case 4 of Table 5.1 showing the shift in the non-linear resonance frequency in the softening-behavior case. Results are shown for $V_{DC} = 0.5$ Volt, $V_{AC} = 0.13$ Volt, and Q = 100. In the figure, $w_{max} = w(1, t)$ is the tip/maximum deflection of a cantilever CNT, (——) stable branch, and (- - - -) unstable branch

CNTs. Figure 5.22 shows a frequency-response curve of a cantilever CNT of case 4 of Table 5.1. The figure shows a weak softening behavior even for large values of V_{AC}.

Next, we show by simulation and using the shooting technique the shift in the resonance frequency Ω_r [79], which is the quantity being measured experimentally and is influenced by the AC amplitude, compared to the linear natural frequency ω_1, which depends on the DC voltage only. Figure 5.23a, b show the variation of the normalized nonlinear resonance frequency Ω_r/ω_1 for clamped-clamped and cantilever

(a) Case 2 of Table 5.1 for (•) $V_{DC}=2$
Volt, and (•) $V_{DC}=5$ Volt.

(b) Case 4 of Table 5.1 for (•) $V_{DC}=0.2$
Volt, and (•) $V_{DC}=0.5$ Volt.

Fig. 5.23 The normalized nonlinear resonance frequency for two cases of CNTs calculated using the shooting technique for $Q = 100$

CNTs, respectively, for various values of AC and DC loads. We can see that the resonance frequency increases considerably with the AC load in the case of hardening behavior for the clamped-clamped CNT but decreases slightly in the case of softening behavior for the cantilever CNT. It is concluded that the strong hardening behavior of the clamped-clamped CNTs makes them almost useless in the linear regime, in agreement with the observation of Postma et al. [3].

Next, we examine the case of the CNT of Fig. 5.23 when V_{DC} is increased to 25 Volt, Fig. 5.24. The figure shows also a hardening-type behavior. In addition, the figure shows that the upper branch of the frequency-response curve opens up and loses stability through a saddle-node bifurcation at an excitation frequency near 28, where its slope approaches infinity and one Floquet multiplier approaches unity. This is an indication of a dynamic pull-in, as has been found for the case of clamped-clamped microbeams [84].

Fig. 5.24 Frequency-response curve of the clamped-clamped carbon nanotube of case 2 of Table 5.1 and for $V_{DC} = 25$ Volt, $V_{AC} = 5$ Volt, and $Q = 100$. In the figure: (——) stable branch, (-----) unstable branch
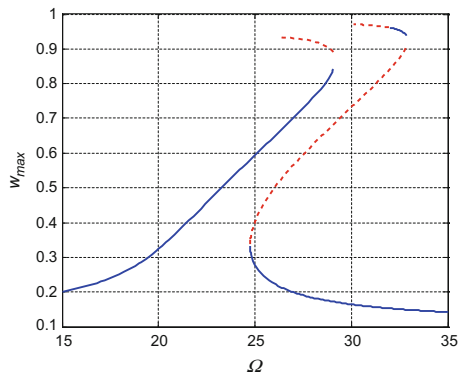
Fig. 5.25 Frequency-
response curve of the
clamped-clamped carbon
nanotube of case 3 of
Table 5.1 and for
$V_{DC} = 100$ Volt,
$V_{AC} = 5$ Volt, and $Q = 100$.
In the figure: (——) stable
branch, (- - - - -) unstable
branch
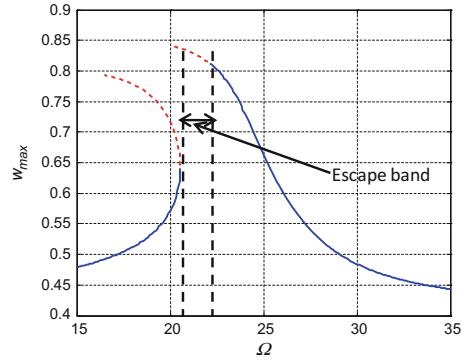
As the value of the DC voltage is increased further, the frequency-response of
the carbon nanotube in this case remains of hardening type until reaching the static
pull-in voltage (it does not reverse to softening behavior as in MEMS microbeams
[84]). This is because in this considered case, the effect of mid-plane stretching is
always dominant over the electrostatic force, except at pull-in. This seems to be a
unique feature for CNTs over other structures.

To demonstrate a softening-type behavior, we choose another case study, case 3
of Table 5.1, where mid-plane stretching has a slightly weaker effect. Hence, at some
DC load before static pull-in value, the electrostatic force nonlinearity dominates that
of mid-plane stretching. Figure 5.25 shows the results. The figure shows a dynamic
pull-in through period doubling bifurcations, where we found a Floquet multiplier
reaching negative one [84, 96]. Figure 5.25 also shows a band of frequencies where
there is no stable solution for the system. This band is called an inevitable escape
band [85], where the oscillator is forced to escape its potential well. In this case the
carbon nanotube is forced to escape to pull-in (see end of Sect. 4.2.2).

Increasing the AC load further in this case results in a larger escape band of
frequencies. We use the shooting technique to calculate the carbon nanotube escape
bands for the primary resonance case while varying the AC voltage and frequency
(instability tongues). Figure 5.26a, b show the results for case 2 of Table 5.1 with
$V_{DC} = 25$ Volt (hardening behavior) and for case 3 of Table 5.1 with $V_{DC} =
100$ Volt (softening behavior), respectively. Operating the resonator within those
instability limits leads to definite pull-in. It is clear also from the figures that if the
AC amplitude increases, the escape band limits increase.

We end this section by investigating the response of cantilever carbon nanotubes.
In this case, the frequency-response curve is always of softening-type because of the
weak effect of the geometric nonlinearity and the strong effect of the electrostatic
nonlinearity. Figure 5.27 shows the frequency-response curve of the carbon nanotube
resonator for case 4 of Table 5.1. The figure shows also a dynamic pull-in through
period doubling bifurcations, where we found Floquet multipliers exceeding the unit
circle through negative one.

(a) Hardening.   (b) Softening.
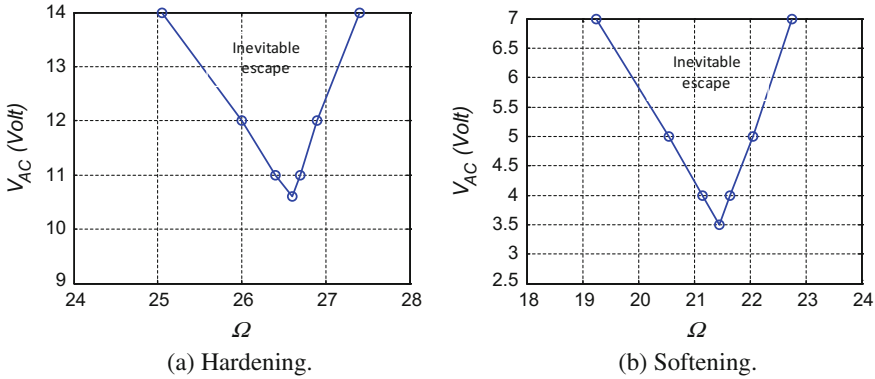
Fig. 5.26 The calculated instability tongues (inevitable escape bands) in the case of primary resonance of a clamped-clamped carbon nanotube (**a**) for the case 2 of Table 5.1 with $V_{DC} = 25$ Volt, (**b**) for the case 3 of Table 5.1 with $V_{DC} = 100$ Volt and $Q = 100$

Fig. 5.27 Frequency-response curve of a cantilever carbon nanotube for case 4 of Table 5.1 and for $V_{DC} = 1\,Volt$, $V_{AC} = 0.1$ Volt, and $Q = 100$. In the figure, $w_{max} = w(1, t)$ is the tip/maximum deflection of the carbon nanotube, (——) stable branch, and (-----) unstable branch
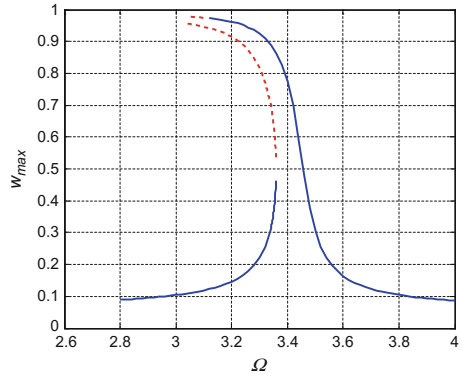

(b) Secondary resonances of the fundamental mode

This section examines the carbon nanotube dynamics near superharmonic resonance of order two (excitation near half the fundamental natural frequency) and subharmonic resonances of order one half and one third (excitation near twice and three times the fundamental natural frequency).

Figure 5.28 shows the response of the clamped-clamped carbon nanotube of case 2 of Table 5.1 when excited near superharmonic resonance of order two of the fundamental mode. The figure shows a hardening-type behavior and a qualitatively similar behavior to that near primary resonance of Fig. 5.24. Also, the figure indicates the occurrence of dynamic pull-in through a saddle-node bifurcation in the upper branch of the curve.

We now examine the response of the same carbon nanotube near subharmonic resonances. It is worth to note that the activation of subharmonic resonance requires exceeding specific thresholds of AC load and quality factor. We excited the carbon nanotube by $V_{DC} = 20$ Volt and $V_{DC} = 1.2$ Volt near twice its natural frequency

Fig. 5.28 Frequency-response curve of the clamped-clamped carbon nanotube for the superharmonic resonance of order two for case 2 of Table 5.1 for $V_{DC} = 20$ Volt, $V_{AC} = 16$ Volt and $Q = 150$. In the figure: (——) stable branch, (-----) unstable branch
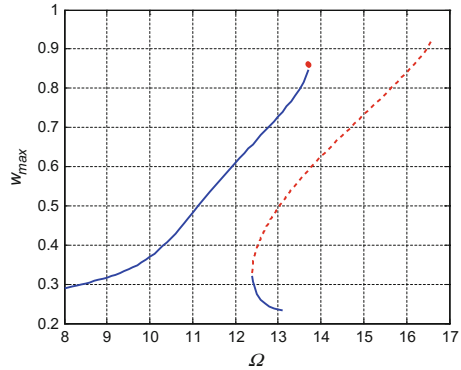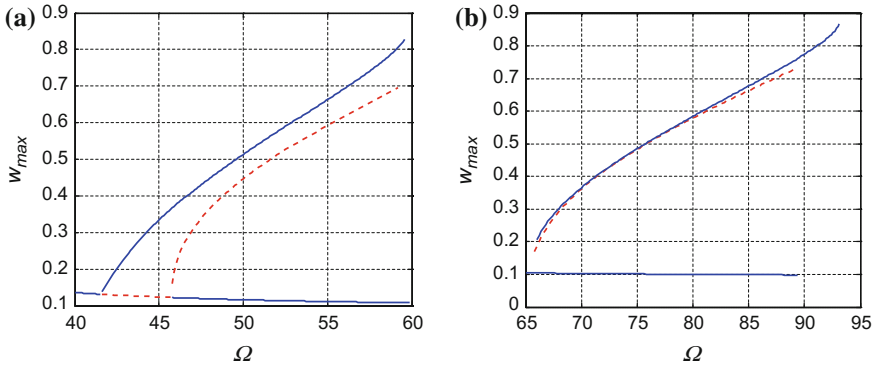

Fig. 5.29 Frequency-response curve for the subharmonic resonance of order one half of the carbon nanotube of case 2 of Table 5.1 for $V_{DC} = 20$ Volt, $V_{AC} = 1.2$ Volt and $Q = 150$. In the figure: (——) stable branch, (-----) unstable branch
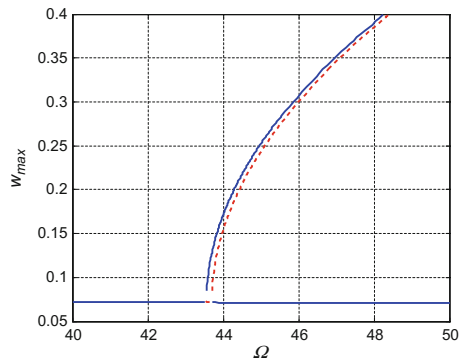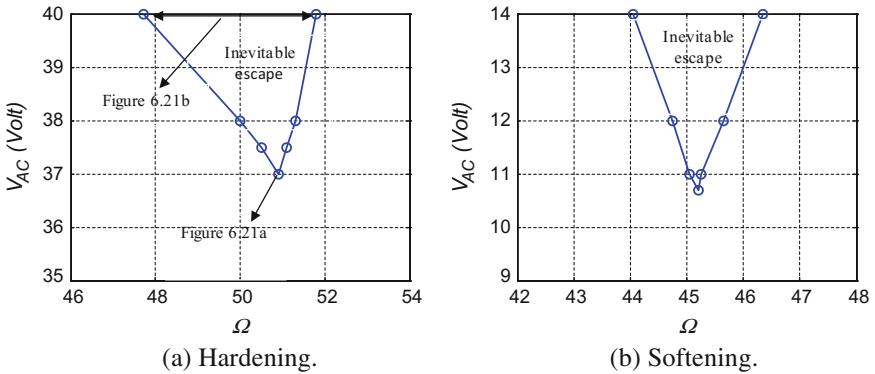

and found that a subharmonic resonance of order one half is activated, Fig. 5.17. Increasing the AC load further to $V_{AC} = 16$ Volt leads to a dynamic pull-in, Fig. 5.30.

Figures 5.28, 5.29, and 5.30a demonstrate secondary resonances of order two and one half due to the influence of the electrostatic force, which is quadratic in nature. However, it is possible also to activate secondary resonances of order one third and three due to the effect of mid-plane stretching, which is cubic in nature. An example of this case is depicted in Fig. 5.30b. Also, in this figure, the curve undergoes dynamic pull-in characterized by a Floquet multiplier approaching unity. One can note from Figs. 5.29 and 5.30 the fact that subharmonic resonance remains activated over a wide range of frequency. This is another significant difference between the dynamics of CNTs and MEMS beams, where subharmonic resonance is activated over a very narrow range of frequency [80].

Next, we use the shooting technique to calculate the inevitable escape bands of frequencies for the subharmonic resonance of order one half while varying the AC voltage and frequency, as we did in the primary resonance case. Figure 5.31a, b show the results for cases 2 and 3 of Table 5.1, respectively. To illustrate the increase in the escape band as the AC voltage increases, the frequency-response curves for the upper and the lower limits of the instability tongue of Fig. 5.31a are depicted in Fig. 5.32a, b, respectively.

Fig. 5.30 Frequency-response curve for the subharmonic resonance of order (**a**) one half and (**b**) one third of the carbon nanotube of case 2 of Table 5.1 for $V_{DC} = 20$ Volt, $V_{AC} = 16$ Volt, and $Q = 150$. In the figure: (——) stable branch, (-----) unstable branch


Fig. 5.31 The calculated instability tongues in the case of subharmonic resonance of order one half (**a**) for case 2 of Table 5.1 with $V_{DC} = 20$ Volt, (**b**) for case 3 of Table 5.1 with $V_{DC} = 100$ Volt and $Q = 150$

Next we show the subharmonic response of a cantilever carbon nanotube. Figure 5.33 depicts a softening-type behavior of the subharmonic resonance of order one half of the fundamental mode. The curve shows dynamic pull-in characterized by period doubling bifurcation.

5.4 Dynamics of Slacked Carbon Nanotube Resonators

In the previous section, we presented a model utilizing a nonlinear beam equation to simulate the static and dynamic behaviors of electrically actuated straight CNT resonators. It is worth to mention that the adopted model does not account for the effect of slack (curvature), buckling, or initial deformation of carbon nanotubes.

(a)

(b)
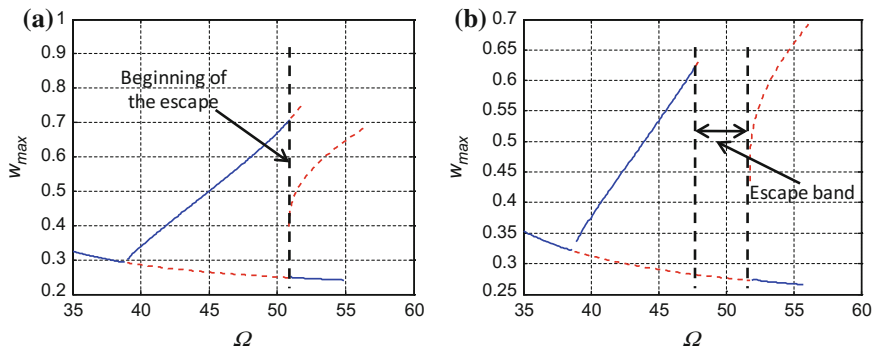
Fig. 5.32 Frequency-response curves for the subharmonic resonance of order one half of the carbon nanotube for case 2 of Table 5.1 when $V_{DC} = 20$ Volt and $Q = 150$ and for (**a**) $V_{AC} = 37$ Volt and (**b**) $V_{AC} = 40$ Volt. In the figure: (——) stable branch and (-----) unstable branch

Fig. 5.33 Frequency-response curve for the subharmonic resonance of order one half of the cantilever carbon nanotube for case 4 of Table 5.1 when $V_{DC} = 1$ Volt, $V_{AC} = 0.2$ Volt, and $Q = 150$. In the figure: (——) stable branch, (-----) unstable branch
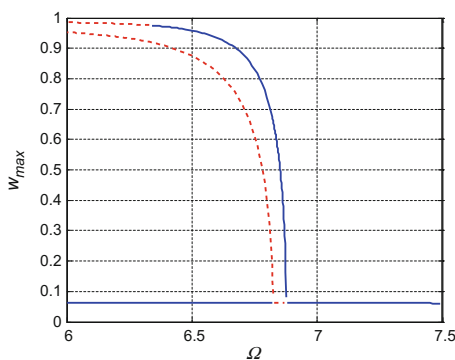
This can have significant influence on the stability, natural frequencies, and pull-in calculations presented so far in the previous chapter. In this section, a 2-D nonlinear curved beam model (arch) is utilized to simulate the motion of a slacked CNT. The variation of the natural frequencies, mode shapes, and effective nonlinearity of a CNT with various levels of slack and DC electrostatic loads is investigated. Various scenarios are shown for mode crossing and mode veering as the levels of slack and DC load are varied. In addition, the forced vibration of the slacked CNT when actuated by small DC and AC loads is analyzed to show the transfer of energy among the vibration modes involved in the veering phenomenon.

5.4.1 Problem Formulation

We start by formulating the 2-D problem governing the static and dynamic behavior of an electrically actuated slacked carbon nanotube resonator, Fig. 5.34. The nanotube
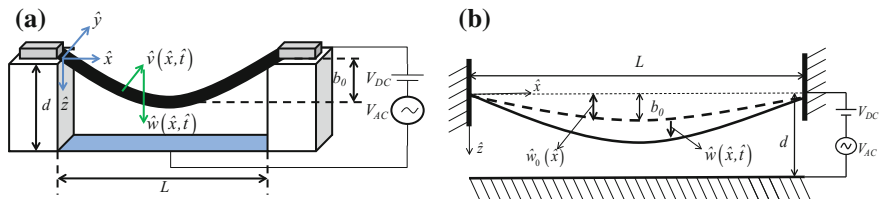
Fig. 5.34 (**a**) 3-D schematic of the electrically actuated slacked carbon nanotube resonator, (**b**) in-plane view of the nanotube

is actuated by an electrode underneath it with a gap width d. It is modeled as a hollow cylinder Euler-Bernoulli beam of radius $\tilde{R}$, shell thickness h, and length L. It has a cross-sectional area A and an area moment of inertia I. The nanotube is assumed to have a Young's modulus $E = 1.2\,TPa$ and a mass density $\rho = 1.3\,\mathrm{g/cm^3}$. The CNT is considered here to be initially curved in the direction of the lower electrode with an initial shape [65].

The 2-D equations describing the in-plane deflection $\hat{w}\left(\hat{x}, \hat{t}\right)$ and out-of-plane deflection $\hat{v}\left(\hat{x}, \hat{t}\right)$ of the clamped-clamped CNT resonator can be written as [69]

$$
EI \frac{\partial^4 \hat{w}}{\partial \hat{x}^4} + \partial A \frac{\partial^2 \hat{w}}{\partial \hat{t}^2} + \tilde{c} \frac{\partial \hat{w}}{\partial \hat{t}} = \hat{F}_{elec} +
$$
$$
+ \frac{EA}{2L} \left[\int_0^L \left\{ \left(\frac{\partial \hat{w}}{\partial \hat{x}}\right)^2 + \left(\frac{\partial \hat{v}}{\partial \hat{x}}\right)^2 - 2\left(\frac{\partial \hat{w}}{\partial \hat{x}} \frac{d\hat{w}_0}{d\hat{x}}\right) \right\} dx \right] \left[\frac{\partial^2 \hat{w}}{\partial \hat{x}^2} - \frac{d^2 \hat{w}_0}{d\hat{x}^2} \right],
$$
$$
(5.101)
$$

$$
EI \frac{\partial^4 \hat{v}}{\partial \hat{x}^4} + \partial A \frac{\partial^2 \hat{v}}{\partial \hat{t}^2} + \tilde{c} \frac{\partial \hat{v}}{\partial \hat{t}} = \frac{EA}{2L} \left[\int_0^L \left\{ \left(\frac{\partial \hat{w}}{\partial \hat{x}}\right)^2 + \left(\frac{\partial \hat{v}}{\partial \hat{x}}\right)^2 - 2\left(\frac{\partial \hat{w}}{\partial \hat{x}} \frac{d\hat{w}_0}{d\hat{x}}\right) \right\} dx \right] \frac{\partial^2 \hat{v}}{\partial \hat{x}^2},
$$
$$
(5.102)
$$

where

$$
\hat{F}_{elec} = \frac{\pi \varepsilon_0 (V_{DC} + V_{AC} \cos(\tilde{\Omega}t))^2}{\sqrt{(d - \hat{w} - \hat{w}_0)(d - \hat{w} - \hat{w}_0 + 2\tilde{R})} \left(\cosh^{-1}\left(1 + \frac{d - \hat{w} - \hat{w}_0}{\tilde{R}}\right)\right)^2},
$$
$$
(5.103)
$$

and where $\tilde{c}$ is the viscous damping coefficient and ε_0 is the air permittivity.

The respective boundary conditions are

$$
\hat{w}\left(0, \hat{t}\right) = 0, \quad \frac{\partial \hat{w}}{\partial \hat{x}}\left(0, \hat{t}\right) = 0, \quad \hat{w}\left(L, \hat{t}\right) = 0, \quad \frac{\partial \hat{w}}{\partial \hat{x}}\left(L, \hat{t}\right) = 0,
$$
$$
(5.104)
$$
$$
\hat{v}\left(0, \hat{t}\right) = 0, \quad \frac{\partial \hat{v}}{\partial \hat{x}}\left(0, \hat{t}\right) = 0, \quad \hat{v}\left(L, \hat{t}\right) = 0, \quad \frac{\partial \hat{v}}{\partial \hat{x}}\left(L, \hat{t}\right) = 0
$$

For convenience, we introduce the following nondimensional variables:

$$w = \frac{\hat{w}}{d}, \qquad v = \frac{\hat{v}}{d}, \qquad x = \frac{\hat{x}}{L}, \qquad t = \frac{\hat{t}}{T}, \qquad (5.105)$$

where T is a time constant defined by $T = \sqrt{(\rho A L^4)/(EI)}$. By substituting Eq. (5.105) into Eqs. (5.101)–(5.104), the nondimensional equations of motions and associated boundary conditions of the considered clamped-clamped CNT are written as

$$\frac{\partial^4 w}{\partial x^4} + \frac{\partial^2 w}{\partial t^2} + \tilde{c}\frac{\partial w}{\partial t} = \alpha_2 F_{elec} + $$
$$+ \alpha_1 \left[\int_0^L \left\{ \left(\frac{\partial w}{\partial x}\right)^2 + \left(\frac{\partial v}{\partial x}\right)^2 - 2\left(\frac{\partial w}{\partial x}\frac{dw_0}{dx}\right) \right\} dx \right] \left[\frac{\partial^2 w}{\partial x^2} - \frac{d^2 w_0}{dx^2} \right],$$
$$(5.106)$$

$$\frac{\partial^4}{\partial x^4} + \frac{\partial^2 v}{\partial t^2} + \tilde{c}\frac{\partial v}{\partial t} = \alpha_1 \left[\int_0^L \left\{ \left(\frac{\partial w}{\partial x}\right)^2 + \left(\frac{\partial v}{\partial x}\right)^2 - 2\left(\frac{\partial w}{\partial x}\frac{dw_0}{dx}\right) \right\} dx \right] \frac{\partial^2 \hat{v}}{\partial x^2},$$
$$(5.107)$$

$$w(0, t) = 0, \quad \frac{\partial w}{\partial x}(0, t) = 0, \quad w(1, t) = 0, \quad \frac{\partial w}{\partial x}(1, t) = 0,$$
$$v(0, t) = 0, \quad \frac{\partial v}{\partial x}(0, t) = 0, \quad v(1, t) = 0, \quad \frac{\partial v}{\partial x}(1, t) = 0,$$
$$(5.108)$$

where

$$F_{else} = \frac{(V_{DC} + V_{AC}\cos(\Omega t))^2}{\sqrt{(1 - w - w_0)(1 - w - w_0 + 2R)} \left(\cosh^{-1}\left(1 + \frac{1 - w - w_0}{R}\right)\right)^2},$$
$$(5.109)$$

$$w_0(x) = \frac{b_o}{d}\sin(\pi x),$$

$$\alpha_1 = \frac{Ad^2}{2I}, \quad \alpha_2 = \frac{\pi\varepsilon_0 L^4}{EId^2}, \quad c = \frac{\tilde{c}L^4}{EIT}, \quad \Omega = \frac{\tilde{\Omega}}{\sqrt{(EI)/(\rho A L^4)}}, \quad R = \frac{\tilde{R}}{d} \quad (5.110)$$

5.4.2 The Reduced-Order Model

To solve the obtained nondimensional equation of motions of the slacked CNT, Eqs. (5.106)–(5.109) are discretized using the Galerkin procedure to yield a ROM. Hence, the in-plane and out-of-plane responses of the CNT are approximated, respectively, as

$$w(x, t) = \sum_{i=1}^{n} u_i(t) \phi_i(x), \quad v(x, t) = \sum_{i=1}^{m} \xi_i(t) \phi_i(x), \quad (5.111)$$

where $\phi_i(x)$ are the normalized linear undamped mode shapes of a straight beam and $u_i(t)$ and $\xi_i(t)$ are the nondimensional modal coordinates of the in-plane and out-of-plane motions, respectively.

To obtain the ROM, we substitute Eq. (5.111) into Eqs. (5.106)–(5.108), multiply by $\phi_i(x)$, use the orthogonality conditions of the mode shapes, and then integrate the outcome from 0 to 1. The results are differential equations in terms of the modal coordinates $u_i(t)$ and $\xi_i(t)$. We should mention here that, as in Sect. 4.3.2, the mode shapes $\phi_i(x)$ will remain embedded inside the denominator of the electrostatic force term, Eq. (5.109), in the ROM. To deal with the complicated integral terms due to that electrostatic force, we evaluate the spatial integrals containing the mode shapes $\phi_i(x)$ numerically simultaneously while integrating the differential equations of the modal coordinates $u_i(t)$ and $\xi_i(t)$.

The Static Response

As a case study, a CNT of $L = 3000$ nm, h $= 0.34$ nm, $\tilde{R} = 1$ nm, $d = 500$ nm, and initial rise $b_o = 100$ nm is considered. Such dimensions are typical of CNTs with slack [4–6]. We have shown in Sect. 4.3 that using one mode only in the ROM is enough to capture the static response of a CNT. Next a one mode is used in the ROM to compare the variation of the maximum in-plane static deflection of the CNT with and without slack, Fig. 5.35.

The figure indicates that for small DC load, the CNT with slack is relatively stiffer due to the linear stiffness term added from the initial curvature. It can be also seen from the figure that the CNT with slack undergoes the pull-in instability at a lower DC load than the one without slack. This is expected since in the slacked configuration, the CNT is nearer to the electrode. Note here that the static response of the out-of-plane motion is zero since the in-plane deflection appears as a homogenous term in the out-of-plane equation (Eq. (5.107)). The stability of the obtained solutions in Fig. 5.35 is studied by calculating the eigenvalues of the Jacobian matrix of the ROM

Fig. 5.35 Variation of the maximum in-plane static deflection of the CNT with the DC voltage for various levels of initial curvature b_0. Solid (——) and dashed (-----) lines denote the stable and unstable branches, respectively
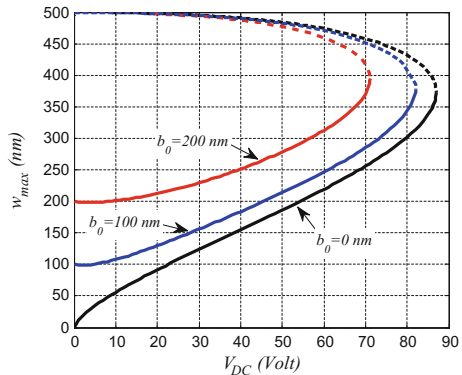
evaluated at these solutions [72]. The results show that one of the eigenvalues of the Jacobian matrix corresponding to the upper branches is always positive indicating unstable solution (dashed line in Fig. 5.35). Also, all of the eigenvalues of the lower branches are pure imaginary indicating stable solutions (continuous line in Fig. 5.35). At pull-in, both stable and unstable branches collide and destroy each other with one eigenvalue tending to zero corresponding to a saddle-node bifurcation.

The Eigenvalue Problem

Next, we investigate the eigenvalue problem of the slacked CNT by calculating the variation of the in-plane and out-of-plane natural frequencies and mode shapes with and without slack and under the actuation of the DC voltage. Toward this, we consider the same procedure of Sect. 4.3.4, where:

$$X = [u_1, u_2, ..., u_n, \xi_1, \xi_2, ..., \xi_m] \qquad (5.112)$$

is the considered modal amplitudes vector.

First, we consider the case study of Üstünel et al. [6], which is a non-hollow CNT of $L = 1750$ nm, $\tilde{R} = 1$ nm, and $d = 500$ nm. For the following results, we will denote the in-plane natural frequencies by ω_i and the out-of-plane frequencies by λ_i. In Fig. 5.36, the variation of the in-plane and out-of-plane natural frequencies is calculated at zero DC load for various values of initial rise of the CNT or slack percentages. The slack percentage is defined as $\%slack = (L - \tilde{L})/L$, where $\tilde{L}$ is the length of the CNT in the deformed (curved) position. Figure 5.36 compares the results with those reported in Üstünel et al. [6], which indicates good qualitative agreement. However, there is a quantitative discrepancy due to the fact that the model used in Üstünel et al. [6] is applicable only when the strain is small enough that the nonlinear elastic effects may be ignored. Unlike their model, our approach

Fig. 5.36 Variation of the first few in-plane and out-of-plane natural frequencies of a CNT with slack for the case study of Üstünel et al. [6]. *Solid line* (——), *dashed line* (-----), and *circles* (○) denote, respectively, the odd in-plane, even in-plane and out-of-plane, and the odd out-of-plane frequencies
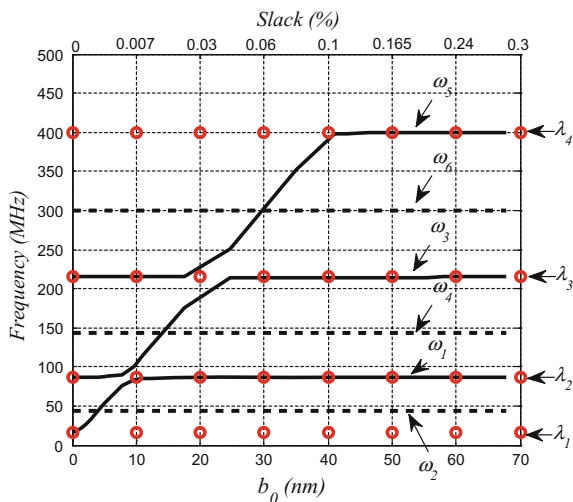
is a continuous model that can describe the nonlinear oscillations of the CNT under its various parameters without dividing the CNT behavior into different regimes.

In Fig. 5.37, we investigate in more depth the effect of varying the initial rise of the CNT of Fig. 5.35, assuming zero DC load, on the in-plane and out-of-plane natural frequencies. We can see clearly that the even in-plane (dashed lines in Fig. 5.37a) and
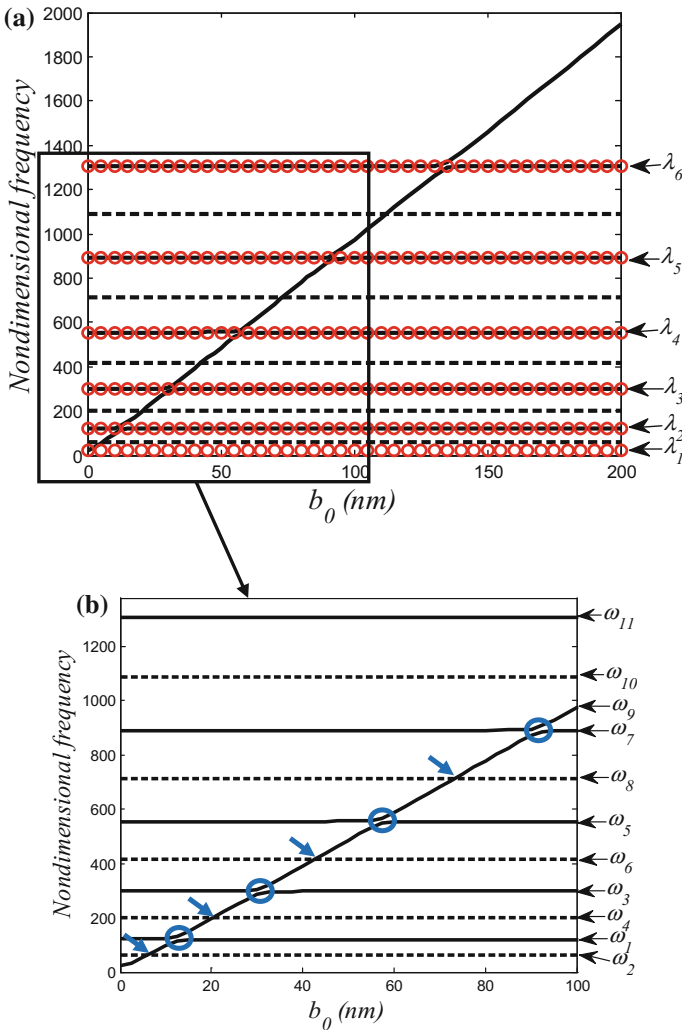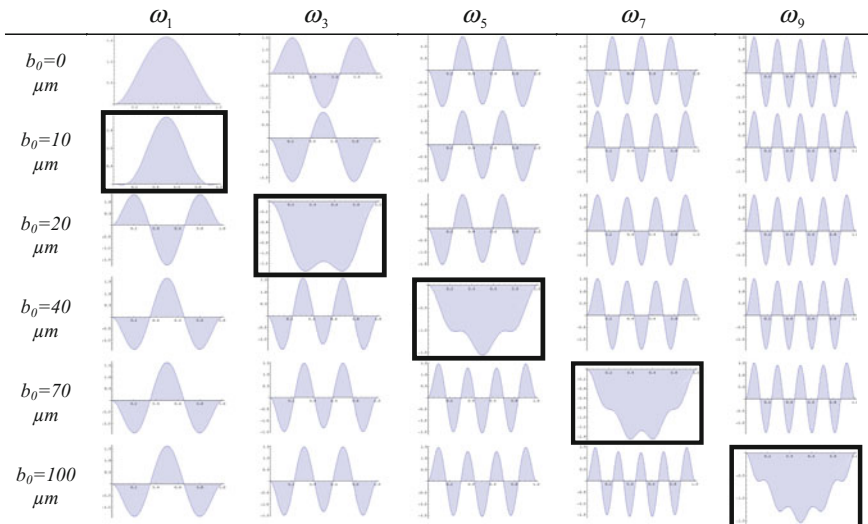

Fig. 5.37 (**a**) Variation of the in-plane and out-of-plane natural frequencies of a CNT with various levels of slack at zero DC load. (**b**) A zoomed view of Fig. 5.4a showing the crossings and veering of the in-plane frequencies (the odd out-of-plane are not shown for clarity). *Solid line* (——), *dashed line* (- - - - -), and circles ($\circ$) denote, respectively, the odd in-plane, the even in-plane and the out-of-plane, and the odd out-of-plane frequencies

out-of-plane frequencies (circles in Fig. 5.37a) are insensitive to the variation of slack whereas the odd in-plane frequencies vary with slack (continuous lines in Fig. 5.37a). These frequencies appear in the large scale to intersect (Fig. 5.37a). When enlarging the apparent intersection zones, one can see that they do not intersect (blue circles in Fig. 5.37b); they diverge in a manner called curve veering [97, 98]. This phenomenon is common and has been cited for the natural frequencies of a rectangular membrane when varying the ratio of its lengths' sides [98] and also for the natural frequencies of cables when varying their sagging levels [99, 100].

A frequency veering occurs when the loci of two eigenvalues, in an eigenvalue problem, approach each other when a parameter is varied and then veer away when being too close like two repulsive charges [101]. In a frequency veering, the eigenfunctions associated with the eigenvalues on each locus before veering is interchanged during the veering [98]. To further clarify this, we plot the corresponding eigenfunctions of the odd in-plane natural frequencies in Table 5.3. We can see that the modes are exchanging shapes and (bold squares in Table 5.3) when varying the slack level. This table describes all the veering scenarios depicted in Fig. 5.37b, which appear following a straight line. In this line, the shape of the first mode is transferred into the different odd modes, from the lower to the higher modes, depending on the slack level. A final note to be mentioned here is that the odd in-plane frequencies intersects the even ones for certain levels of slack offering many possibilities of internal resonances and exchange of energy among higher- and lower-order modes.

Table 5.3 The simulated eigenfunctions of the first five odd in-plane modes for various slack levels
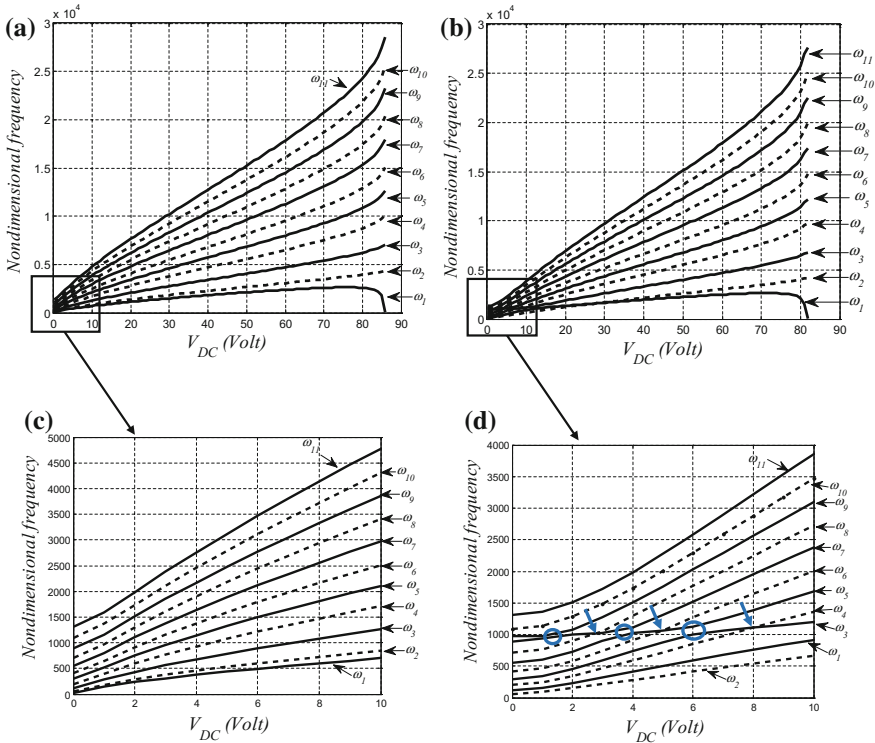
Fig. 5.38 (**a**) Variation of the in-plane natural frequencies with the DC load of a CNT (**a**) without and (**b**) with slack. In both cases, a zoomed view near small values of voltages are shown (**c**) and (**d**). *Solid line* (——) and *dashed line* (- - - - -) denote the odd in-plane and the even in-plane frequencies, respectively

Next we investigate the variation of the in-plane natural frequencies of the CNT with the DC load. First, we consider the unslacked case. We can see from Fig. 5.38a that all the natural frequencies are sensitive to the variation of the DC voltage. All of them are increasing dramatically, with a sublinear variation behavior, except for the first frequency near pull-in where it drops to zero. This increase in the frequencies suggests a tunable resonator over a wide range of frequencies. Practically, when designing a resonator made with such CNT, one can easily tune the frequencies from MHz range to GHz and even THz range. In addition, one can see from Fig. 5.38c that there is no possibility of modes veering or modes crossing even for small range of voltages. These scenarios however appear when slack is added, Fig. 5.38b. The figure shows the variation of the first few in-plane frequencies of the slacked CNT ($b_0 = 100$ nm) with the DC load. We can see that the odd modes exhibit the frequency veering phenomenon (blue circles in Fig. 5.38d), but in this case from the higher to the lower modes where the energy is transferred to the lowest fundamental frequency that eventually drops to zero at pull-in. There are also possibilities of odd and even in-plane modes crossings (blue arrows in Fig. 5.38d).

It is worth to mention here that our demonstrated results can justify and predict some of observed experimentally phenomena in Sazanova [5]. Other models of [5, 6] could not explain the previously mentioned phenomenon. For example, Fig. 5.38 shows what was cited as sublinear dispersion of the frequency in Sazanova [5]. The avoided crossings for some frequency range in the case of slack cited in Sazanova [5], can be considered to be the same as veering, Fig. 5.39. Also, our results, based on the coupled in-plane and out-of-plane motions, have shown abundance of resonances as cited in Sazanova [5].

Next, we investigate the sensitivity of the out-of-plane natural frequencies to the DC load, which although not directly actuated, they are affected due to the nonlinear coupling between the out-of-plane and in-plane deflections. Figure 5.39 shows the first five in-plane and out-of plane natural frequencies as they vary with the DC load. We can note that, except for the first mode, the first few out-of-plane frequencies are larger than those of the in-plane frequencies especially at high DC loads. For the higher-order modes, both in-plane and out-of-plane natural frequencies are equal.

5.4.3   The Dynamic Response for Small DC and AC Loads

(a) Long-time integration of the ROM

Next, we use the ROM developed in Sect. 4.4.2 to integrate the differential equations of motion in time to obtain the dynamic response of the slacked CNT under a very small DC and AC harmonic load. The choice of the very small voltage loads is to guarantee linear forced vibration response. The response to small electric loads is important to enable precise prediction of the resonance frequency in the linear regime. The resonance frequency is the frequency that is commonly measured experimentally for CNTs when driven by AC and DC loads. Here we use a nondimensional damping coefficient c = 1.196. Figure 5.40a, b show the response of the 100 nm and the 200 nm slacked CNTs, respectively. We can see from the figures that the linear dynamic response is significant in the neighborhood of the first natural frequency, ω_1, and the frequencies that are located on the veering straight line, as predicted from Fig. 5.37. Those frequencies are ω_9 in the case of the 100 nm slack and ω_{11} in the case of the 200 nm slack. It is clear from Fig. 5.40a, b that the higher-order modes located on the veering line are sharing the energy of vibration with the fundamental mode. This conclusion might explain one of the reasons behind the low quality factor reported experimentally for CNTs [5] when driven harmonically at resonance near their fundamental modes.

To further clarify this point, we calculate in Fig. 5.41 the participation of each individual odd in-plane mode shape in the dynamic response of the 100 nm slacked CNT. It is clear from the figure that the participations of the first mode (the lowest mode) and the ninth mode (the one located on the veering line) are the most important ones. This indicates that even when exciting the CNT near its first natural frequency, significant participation is anticipated of the mode located on the veering line.
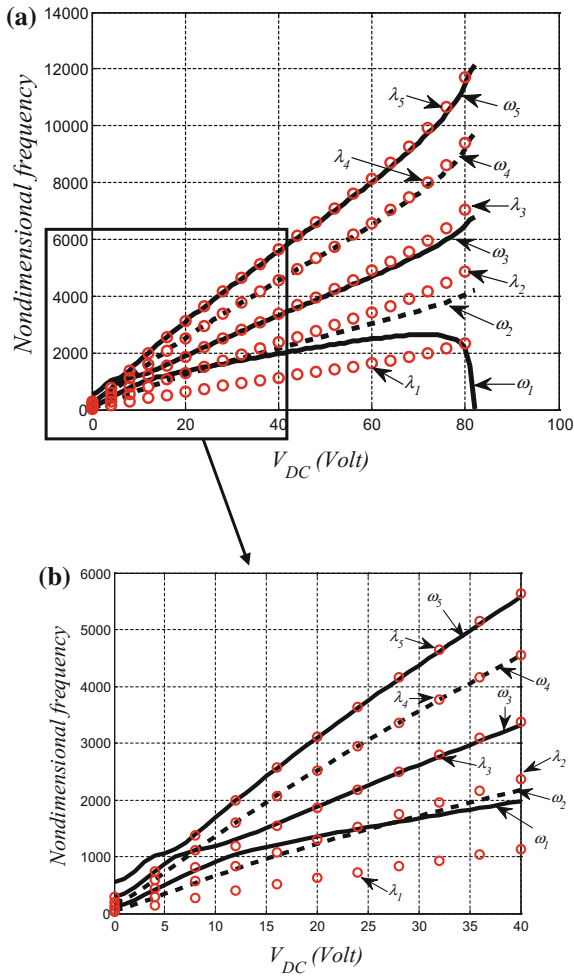
Fig. 5.39 a Variation of the first five in-plane and out-of-plane natural frequencies with the DC load of a CNT with a 100 nm slack. **b** A zoomed view of Fig. 5.39a near small values of voltages. *Solid line* (——), *dashed line* (-----), and circles (○) denote, respectively, the odd in-plane, the even in-plane and the out-of-plane, and the odd out-of-plane frequencies

## (b) Perturbation analysis

(i) Derivations

In this section, perturbation analysis is carried out using the method of multiple scales and a direct attack of the in-plane equations of motion same as we did in Sect. 4.5.1. To this end, we define the variables for the time scale (T_i), their derivatives (D_i), the influence of the damping coefficient and the forcing amplitude, as in Eqs. (4.117)
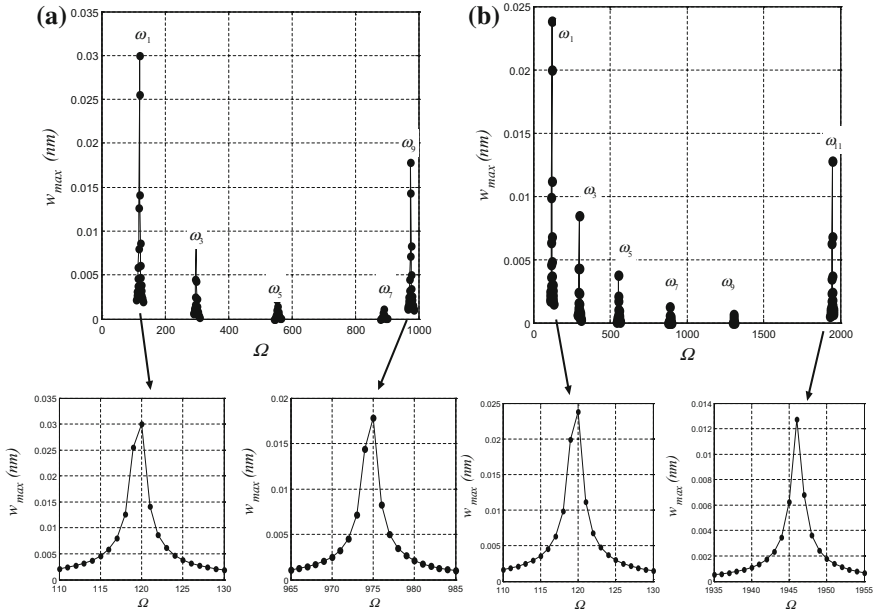
Fig. 5.40 Frequency-response curves of (**a**) 100 nm slacked CNT and (**b**) 200 nm slacked CNT at the odd in-plane natural frequencies. Results are shown for $V_{DC} = 0.01$ Volt, $V_{AC} = 0.01$ Volt, and 100 quality factor
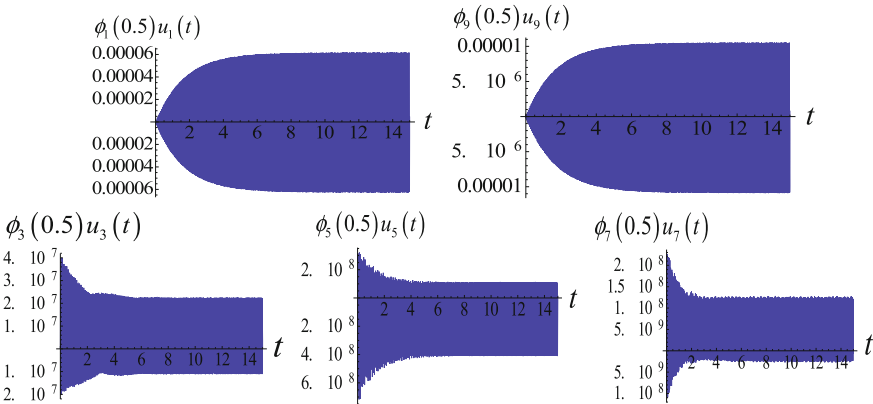
Fig. 5.41 Time-response curves of the 100 nm slacked CNT at $\Omega \approx \omega_1$ showing the participation of the odd in-plane mode shapes. Results are shown for $V_{DC} = 0.01$ Volt, $V_{AC} = 0.01$ Volt, and 100 quality factor

and (4.118) respectively, and we seek a solution in the form of Eq. (4.119). Next, we expand the electrostatic force term, Eq. (5.109), into Taylor series up to the third order as

$$\frac{1}{\sqrt{(1 - u - w_s - w_0)(1 - u - w_s - w_0 + 2\tilde{R})} \left(\cosh^{-1} \left(1 + \frac{1 - u - w_s - w_0}{\tilde{R}} \right) \right)^2} \approx \quad (5.113)$$

$$\approx F_s + F_1 u + F_2 u^2 + F_3 u^3 + \cdots,$$

Substituting Eqs. (4.117)–(4.120) and Eq. (5.113) into Eqs. (5.106) and (5.108) and then equating like powers of ε, we obtain

- **Order ε^0: (the static equation)**

$$w_s^{iv} = \alpha_1 [w_s'' - w_0''][\Gamma(w_s, w_s) - 2\Gamma(w_s, w_0)] + F_s,$$
$$w_s(0) = w_s(1) = 0, \qquad w_s'(0) = w_s'(1) = 0, \quad (5.114)$$

- **Order ε^1:**

$$L(u_1) = D_0^2 u_1 + u_1^{iv} - \alpha_1 [\Gamma(w_s, w_s) - 2\Gamma(w_s, w_0)] u_1''$$
$$-2\alpha_1 [w_s'' - w_0''][\Gamma(w_s, u_1) - \Gamma(w_0, u_1)] - \alpha_2 F_1 u_1 = 0, \quad (5.115)$$

- **Orderε^2:**

$$L(u_2) = \alpha_1 \Gamma(u_1, u_1)\left(w_s'' - w_0''\right) + 2\alpha_1 [\Gamma(w_s, u_1) - \Gamma(w_0, u_1)] u_1'' + F_2 u_1^2, \quad (5.116)$$

- **Order ε^3:**

$$L(u_3) = -2D_0 D_2 u_1 - cD_0 u_1 + 2\alpha_1 \Gamma(u_1, u_2)\left(w_s'' - w_0''\right)$$
$$+2\alpha_1 [\Gamma(w_s, u_1) - \Gamma(w_0, u_1)] u_2''$$
$$+2\alpha_1 [\Gamma(w_s, u_2) - \Gamma(w_0, u_2)] u_1'' + \alpha_1 \Gamma(u_1, u_1) u_1'' \quad (5.117)$$
$$+2\alpha_2 V_{DC} V_{AC} F_s \cos(\Omega t) + \alpha_2 F_2 u_1 u_2 + \alpha_2 F_1 u_1^3,$$

The solution of Eq. (5.115) is assumed to consist of only the directly excited mode, $\Phi_i(x)$, because in the absence of internal resonances, all the other modes die out with the damping [102]. Accordingly, we express the first dynamic component u_1 as

$$u_1(x, T_0, T_2) = \left[A(T_2) e^{i\omega_i T_0} + \bar{A}(T_2) e^{-i\omega_i T_0} \right] \Phi_i(x), \quad (5.118)$$

where $A(T_2)$ is a complex-valued function, the over bar denotes the complex conjugate, and ω_i and $\Phi_i(x)$ are the natural frequency and corresponding eigenfunction of the directly excited mode, respectively. Substituting Eq. (5.118) into Eq. (5.16), we obtain

$$L(u_2) = \left(2A\bar{A} + A^2 e^{2i\omega_i T_0} + \bar{A}^2 e^{-2i\omega_i T_0} \right) h(x), \quad (5.119)$$

where

$$h(x) = 2\alpha_1 \left(\Gamma(w_s, \Phi_i) - \Gamma(w_0, \Phi_i) \right) \Phi_i'' +$$
$$+\alpha_1 \Gamma(\Phi_i, \Phi_i)\left(w_s'' - w_0''\right) + \alpha_2 F_2 \Phi_i^2, \quad (5.120)$$

The solution of Eq. (5.119) can be expressed as follows:

$$
\begin{aligned}
u_2(x, T_0, T_2) &= \psi_1(x) A^2(T_2) e^{2i\omega_i T_0} + \\
&+ 2\psi_2(x) A(T_2)\bar{A}(T_2) + \psi_1(x)\bar{A}^2(T_2) e^{-2i\omega_i T_0},
\end{aligned}
\tag{5.121}
$$

where ψ_1 and ψ_2 are the solutions of the following boundary value problems:

$$
\begin{aligned}
H\left(\psi_j, 2\omega_i \delta_{1j}\right) &= h(x), \quad j = 1, 2, \\
\psi_j = 0 \text{ and } \psi_j' &= 0 \text{ at } x = 0 \text{ and } x = 1, \quad j = 1, 2,
\end{aligned}
\tag{5.122}
$$

where δ_{ij} is the Kronecker delta operator and the linear differential operator H is defined as

$$
\begin{aligned}
H(f(x), \omega) &= f^{iv}(x) - \omega^2 f(x) \\
&\quad - 2\alpha_1 \left(w_s'' - w_0''\right) \left[\Gamma(f(x), w_s) - \Gamma(f(x), w_0)\right] \\
&\quad - \alpha_1 \left[\Gamma(w_s, w_s) - 2\Gamma(w_0, w_s)\right] f''(x) - \alpha_2 F_1 f(x)
\end{aligned}
\tag{5.123}
$$

Note here that the eigenfunction $\Phi_i(x)$ is solution of

$$
H(\Phi_i, \omega) = 0,
\tag{5.124}
$$

In order to describe the nearness of the excitation frequency Ω to the fundamental natural frequency ω_i, we introduce a detuning parameter σ defined by

$$
\Omega = \omega_i + \varepsilon^2 \sigma,
\tag{5.125}
$$

Substituting Eqs. (5.118), (5.121), and (5.125) into Eq. (5.117) we obtain

$$
L(u_3) = \left[-i\omega_i \left(2A' + cA\right) \Phi_i(x) + \chi(x) A^2\bar{A} + \bar{F}(x) e^{i\sigma T_2}\right] e^{i\omega_i T_0} + cc + NST,
\tag{5.126}
$$

where

$$
\bar{F}(x) = 2\alpha_2 V_{\text{DC}} V_{\text{AC}} F_s
\tag{5.127}
$$

In Eq. (5.126), A' denotes the derivative of A with respect to T_2, "cc" denotes the complex conjugate of the preceding terms, NST stands for the terms that do not produce secular terms, and $\chi(x)$ is defined by

$$
\begin{aligned}
\chi(x) &= \alpha_1 \Phi_i'' \left[3\Gamma(\Phi_i, \Phi_i) + 2\Gamma(w_s, \psi_1) - 2\Gamma(w_0, \psi_1) + 4\Gamma(w_s, \psi_2) - 4\Gamma(w_0, \psi_2)\right] \\
&\quad + \alpha_1 \left[w_s'' - w_0''\right] \left[2\Gamma(\Phi_i, \psi_1) + 4\Gamma(\Phi_i, \psi_2)\right] \\
&\quad + 2\alpha_1 \left[\psi_1'' + 2\psi_2''\right] \left[\Gamma(\Phi_i, w_s) - \Gamma(\Phi_i, w_0)\right] \\
&\quad + 3\alpha_2 F_3 \Phi_i^3 + 2\alpha_2 F_2 \Phi_i \psi_1 + 4\alpha_2 F_2 \Phi_i \psi_2,
\end{aligned}
\tag{5.128}
$$

Note that the function $\chi(x)$ can be divided into two coefficients that describe the two sources of nonlinearity presented in the considered electrically actuated CNT slacked resonator as follows:

$$\chi(x) = \chi_c(x) + \chi_q(x), \tag{5.129}$$

where

$$
\begin{aligned}
\chi_c(x) &= 3\alpha_1 \Phi_i'' \Gamma(\Phi_i, \Phi_i) + 3\alpha_2 F_3 \Phi_i^3, \\
\chi_q(x) &= 3\alpha_1 \Phi_i'' \left[2\Gamma(w_s, \psi_1) - 2\Gamma(w_0, \psi_1) + 4\Gamma(w_s, \psi_2) - 4\Gamma(w_0, \psi_2)\right] + \\
&\quad + \alpha_1 \left[w_s'' - w_0''\right]\left[2\Gamma(\Phi_i, \psi_1) + 4\Gamma(\Phi_i, \psi_2)\right] + \\
&\quad + 2\alpha_1 \left[\psi_1'' + 2\psi_2''\right]\left[\Gamma(\Phi_i, w_s) - \Gamma(\Phi_i, w_0)\right] + \\
&\quad + 2\alpha_2 F_2 \Phi_i \psi_1 + 4\alpha_2 F_2 \Phi_i \psi_2.
\end{aligned}
\tag{5.130}
$$

The subscripts c and q denote the cubic nonlinear term and the quadratic nonlinear term, respectively.

Next, multiplying the right-hand side of Eq. (5.126) by $\Phi_i(x) e^{-i\omega_i T_0}$, where Φ_i is normalized such that $\int_0^1 \Phi_i^2 dx = 1$, integrating the result from $x = 0$ to $x = 1$ and equating the secular terms to zero, yields the following solvability condition:

$$-i\omega\left(2A' + cA\right) + SA^2\bar{A} + Fe^{i\sigma T_2} = 0, \tag{5.131}$$

where

$$F = \int_0^1 \Phi_i \bar{F} dx, \text{ and } S = S_c + S_q, \tag{5.132}$$

where the nonlinear coefficients are expressed as

$$S_c = \int_0^1 \Phi_i \chi_c dx, \ S_q = \int_0^1 \Phi_i \chi_q dx \tag{5.133}$$

Next, we express A in the polar form $A = ae^{i\beta}/2$, where $a = a(T_2)$ and $\beta = \beta(T_2)$ are real-valued functions, representing, respectively, the amplitude and phase of the response. Substituting the expression of A into Equation (5.31) and letting $\gamma = \sigma T_2 - \beta$, we obtain

$$\left[\left(-ia' + a\beta' - \frac{1}{2}ica\right)\omega_i + \left(\frac{a^3}{8}\right)S\right]e^{i\beta} + Fe^{i\sigma T_2} = 0 \tag{5.134}$$

Separating the real and imaginary parts in Eq. (5.134), we obtain the following modulation equations:

$$a' = -\frac{1}{2}ca + \frac{\sin\gamma}{\omega_i}F, \tag{5.135}$$

$$a\gamma' = a\sigma + \frac{a^3}{8\omega_i}S + \frac{\cos\gamma}{\omega_i}F \tag{5.136}$$

Substituting Eqs. (5.118) and (5.121) into the Method of Multiple Scales approximated solution and setting $\varepsilon = 1$, we obtain, to the second-order approximation, the following CNT response to the external excitation as follows:

$$w(x,t) = w_s(x) + a\cos(\Omega t - \gamma)\Phi_i(x) + \\ + \tfrac{1}{2}a^2\left[\psi_1(x)\cos 2(\Omega t - \gamma) + \psi_2(x)\right] + \cdots, \tag{5.137}$$

It follows from Eq. (5.137) that periodic solutions correspond to constant a and γ; that is, the fixed points (a_0, γ_0) of Eqs. (5.135) and (5.136). Thus, letting $\gamma' = 0$ and $a' = 0$ in Eqs. (5.135) and (5.136), and eliminating γ_0 yield the following frequency-response equation:

$$\frac{F^2}{\omega_i^2} = a_0^2\left[\left(\sigma + \frac{a_0^2}{8\omega_i}S\right)^2 + \frac{1}{4}c^2\right], \tag{5.138}$$

where $c = 2\zeta\omega_i$.

(ii) Results

As seen before when analyzing the dynamic behavior of MEMS arches, the important advantage of the perturbation analysis described above is that it enables studying the variation of the effective nonlinearity of the system and its quadratic and cubic components analytically. To calculate the variation of the effective nonlinearity of the slacked CNT along with its two cubic and quadratic nonlinear components, we evaluate numerically the parameters ω_i, Φ_i, ψ_1, ψ_2, and w_s associated with Eq. (5.132) using a ROM similar to what has been done in Sect. 4.3.3.

First, motivated by studying the effect of the DC load on the CNT nonlinearity for various unslacked CNT radiuses, we calculate its effective nonlinearity variation with the electric load for three different radiuses (10, 20, and 30 nm) of a non-hallow CNT of $L = 1000$ nm, $d = 100$ nm, Young modulus $E = 1\,TPa$, and mass density $\rho = 1.3\,\mathrm{g/cm^3}$, Fig. 5.42. The figure shows clearly that the percentage of the DC load needed to switch from a hardening behavior to a softening one over the pull-in value increases with the increase of the CNT radius. This percentage is calculated to be 16 % for the CNT of 10 nm radius, 43 % for the CNT of 20 nm radius, and 65 % for the CNT of 30 nm radius. One clear possibility of this behavior is that with the increase of the CNT radius, the ratio of the nondimentional cubic nonlinearity parameter over the quadratic one of Eq. (5.106), i.e. α_1/α_2, increases and hence letting the hardening behavior becoming more dominant for CNT with large radius. Add to all of this, we can see clearly that with the increase of the CNT radius, the increase of the cubic nonlinear coefficient (S_c), which turns out to be more dominant over a wide range of DC load. For those cases, the effective nonlinearity switches from positive to negative only when the quadratic nonlinear terms (S_q) starts to vary with the DC load. This coefficient starts to vary for small DC load compared to the DC pull-in value for
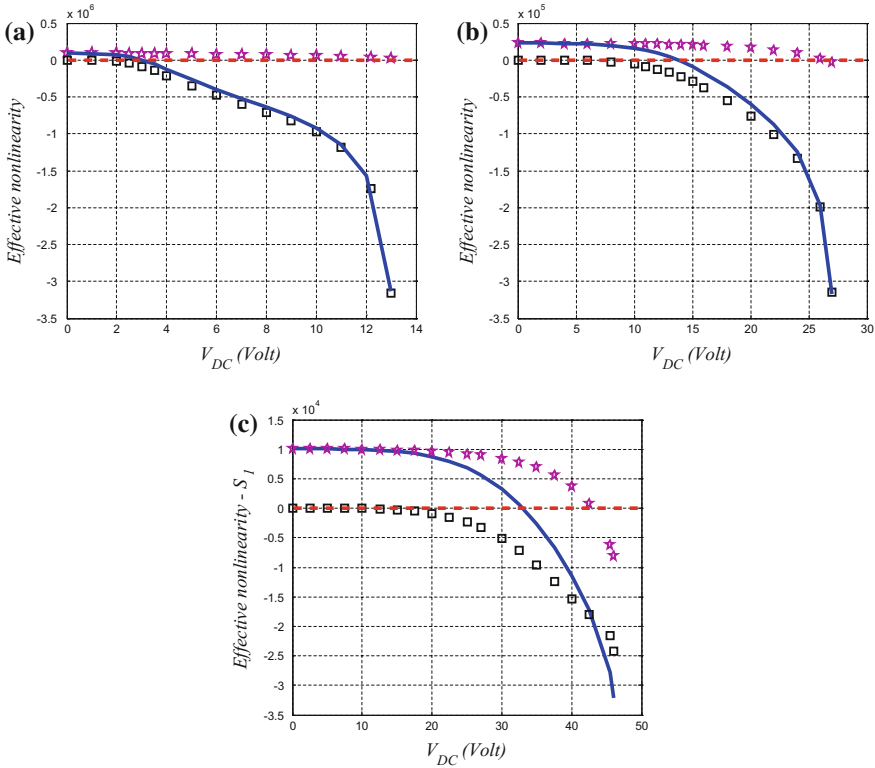
Fig. 5.42 Variation of the effective nonlinearity of the fundamental mode (——), the cubic nonlinearity coefficient (☆), and the quadratic nonlinearity coefficient (□) for an unslacked CNT with the DC voltage: **a** $\tilde{R} = 10$ nm, **b** $\tilde{R} = 20$ nm, and (**c**) $\tilde{R} = 30$ nm. The *dashed line* (-----) separates the positive and the negative regimes of the effective nonlinearity describing, respectively, the hardening and the softening behaviors of the CNT

smaller CNT radius and vice versa. Those trends explain clearly the difference in the dynamical behavior between CNT with small radius (high aspect ratio) and those with high radius (small aspect ratio).

Next, as a case study for slacked CNT, a non-hallow CNT of $L = 1000$ nm, $\tilde{R} = 5$ nm, $d = 200$ nm, $E = 1$ TPa, and $\rho = 1.3$ g/cm^3 is considered. In Fig. 5.43, we show the variation of the effective nonlinearity coefficient of the fundamental mode (S) of the CNT with the slack. For the case of small slack ($b_o < 4$ nm), S is positive indicating a hardening behavior and then it switches to negative sign ($b_o > 4$ nm) indicating softening-type behavior. Dynamically point of view, this indicates that for tiny slack level, the CNT is locally dominated by a softening type behavior which means that the quadratic nonlinearity coming from the initial curvature dominates the dynamic behavior of the slacked CNT (S_q is dominant for high values of b_o).

Fig. 5.43 a Variation of the
effective nonlinearity of the
fundamental mode (——), the
cubic nonlinearity coefficient
($\star$), and the quadratic
nonlinearity coefficient ($\square$)
of the CNT with the slack
level. **b** A zoomed view of
Fig. 5.43a showing the
switch of the effective
nonlinearity from positive to
negative values
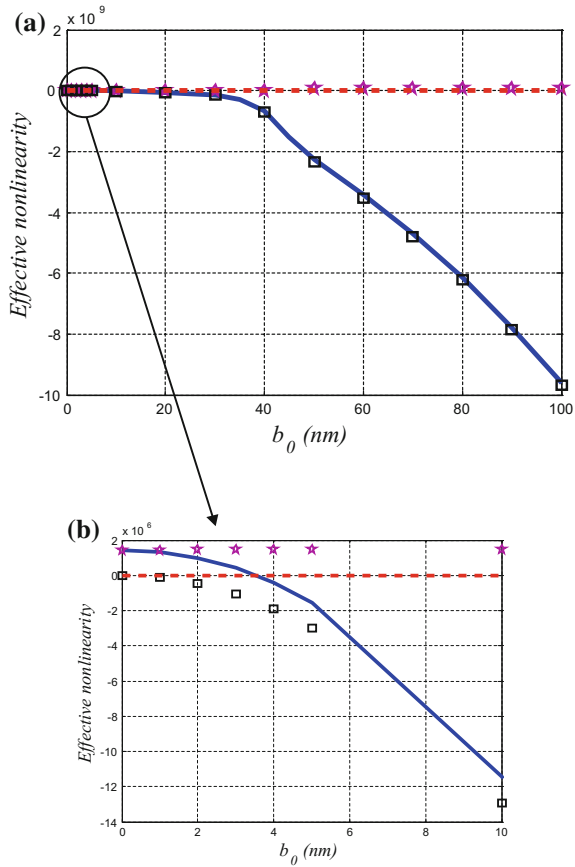
To verify the results of Fig. 5.43, we use the ROM developed in Sect. 6.2 and integrate with time the differential equations of motion to obtain the forced response of the slacked CNT under small DC voltage and an AC harmonic load. Figure 5.44a, b show the responses of a 2 nm and 5 nm slacked CNT, respectively. We can see from the figures that the dynamic response of the CNT switched from being hardening for the first case to softening for the second case confirming what was found in Fig. 5.43.

Next, we show the variation of the effective nonlinearity coefficient (S) of the CNT as well as the nonlinear coefficients with DC load for the case of no initial curvature, Fig. 5.45. For small DC load ($V_{DC} < 10$ nm), S is positive indicating a hardening behavior and then it switches to negative sign ($V_{DC} > 10$ nm) indicating softening type behavior, Fig. 5.45. This shows that the considered CNT is dominated by a softening once the DC load exceeds a small voltage compared to the pull-in value. Here we also generate frequency-response curves based on the ROM, Fig. 5.46, to verify the results of Fig. 5.45.
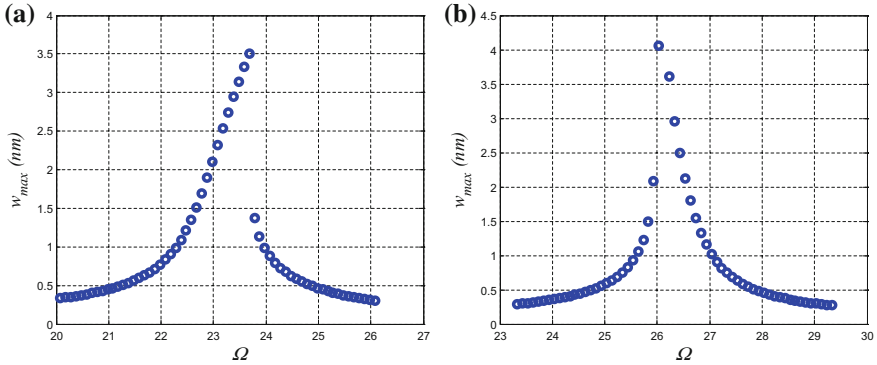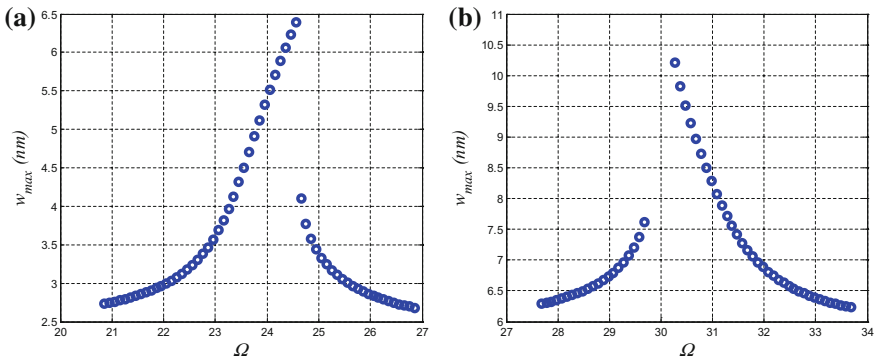
Fig. 5.44 Frequency-response curves of (**a**) 2 nm and (**b**) 5 nm slacked CNT showing hardening and softening behaviors, respectively. Results are shown for $V_{DC} = V_{AC} = 1$ Volt, and 100 quality factor
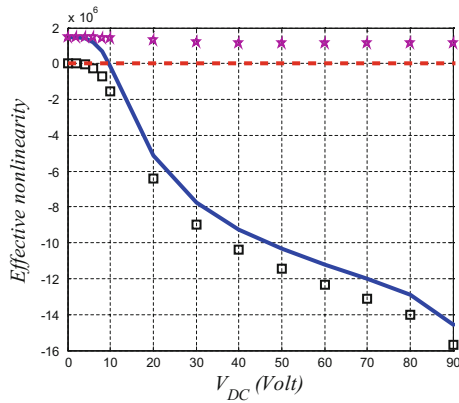

Fig. 5.45 Variation of the effective nonlinearity of the fundamental mode (——), the cubic nonlinearity coefficient (☆), and the quadratic nonlinearity coefficient (□) of the unslacked CNT with the DC voltage

Figure 5.47 shows that for nonzero slack (80 nm), S is always negative, with an increase except near the pull-in zone, indicating a softening type behavior of the slacked CNT. This result indicates the fundamental mode of a slacked CNT is locally dominated by a softening type behavior demonstrating that the quadratic nonlinearities coming from the initial curvature and the electrostatic force dominate the dynamic behavior of the slacked CNT.

(a)

(b)

Fig. 5.46 Frequency-response curves of unslacked CNT for (**a**) $V_{DC} = 8$ Volt, and (b) $V_{DC} = 14$ Volt showing hardening and softening behaviors respectively. Results are shown for $V_{AC} = 0.2$ Volt, and 100 quality factor

Fig. 5.47 Variation of the effective nonlinearity of the fundamental mode (——), the cubic nonlinearity coefficient (☆), and the quadratic nonlinearity coefficient (□) for the 80 nm slacked CNT with the DC voltage
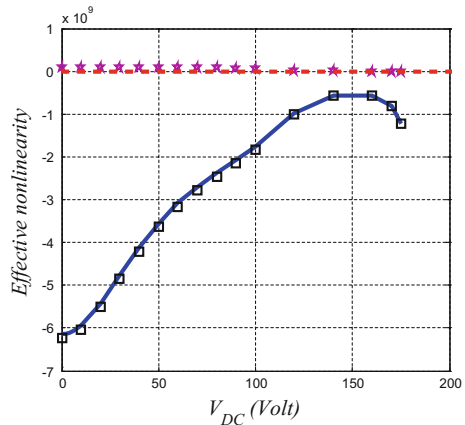
5.4.4 The String Model

(a) Motivation and formulation

For some specific CNT geometry, especially those with small radius (i.e., with big aspect ratio), the beam model experiences some numerical problems especially when trying to solve the boundary value problems of Eqs. (5.126)–(5.128). The algorithm that we used to calculate the effective nonlinearity coefficient based on the beam model of Sect. 4.4.1 works only for small DC load (i.e., the bending dominated regime). This is expected since, for the case of CNT with small radius, the bending term is dominant only for small DC load [4, 6]. Hence, we propose to use a string model, in which we eliminate the bending term in Eq. (5.106). This yields the following nondimentional equation of motion and associated boundary conditions:

$$\frac{\partial^2 w}{\partial t^2} + c \frac{\partial w}{\partial t} = \alpha_2 F_e + \alpha_1 \left[\int_0^1 \left\{ \left(\frac{\partial w}{\partial x} \right)^2 - 2 \left(\frac{\partial w}{\partial x} \frac{dw_0}{dx} \right) \right\} dx \right] \left[\frac{\partial^2 w}{\partial x^2} - \frac{d^2 w_0}{dx^2} \right], \quad (5.139)$$

$$w(0, t) = 0, \quad w(1, t) = 0, \quad (5.140)$$

where F_e and w_0 are given by Eq. (5.109), and the nondimensional parameters are defined as

$$\alpha_1 = \frac{EAd^2}{2L^2}, \quad \alpha_2 = \frac{\pi \varepsilon_0 L^2}{d^2}, \quad c = \frac{\tilde{c}}{\sqrt{\rho A L^2}}, \quad \Omega = \tilde{\Omega} \sqrt{\rho A L^2}, \quad R = \frac{\tilde{R}}{d} \quad (5.141)$$
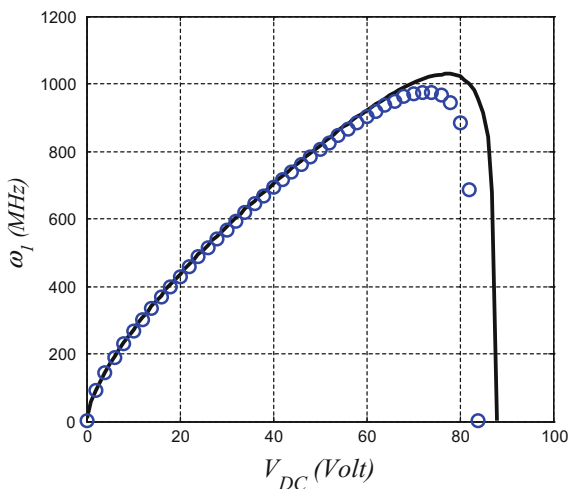
(b) Results

As a case study for a CNT with small radius and high aspect ratio, a hallow CNT of $L = 3000$ nm, $h = 0.34$ nm, $\tilde{R} = 1$ nm, $d = 500$ nm, $E = 1.2$ TPa, and $\rho = 1.35$ g/cm^3 is considered.

We first compare between the dimensional fundamental natural frequency of the considered CNT with small radius while using both models (the beam and the string models). One can see from Fig. 5.48 that for a wide range of DC load (5 Volt < V_{DC} < 60 Volt), between the bending dominated regime and the pull-in zone, the string and the beam model are in a good agreement. Hence, we will use now the perturbation analysis derived in Sect. 4.4.5b while considering the beam model for small DC load, and use the string model for higher values of the DC load.

Next, we simulate the variation of the effective nonlinearity with the curvature level. In this case, the beam model is used since the nonlinearity coming from the electrostatic load is small. We can see from Fig. 5.49 that S is positive in this case for very small range of initial curvature level ($b_o < 1$ nm) indicating a hardening

Fig. 5.48 Comparison between the variations of the dimensional fundamental natural frequency of the unslacked CNT with the DC voltage using the beam model (——) and the string model (○)
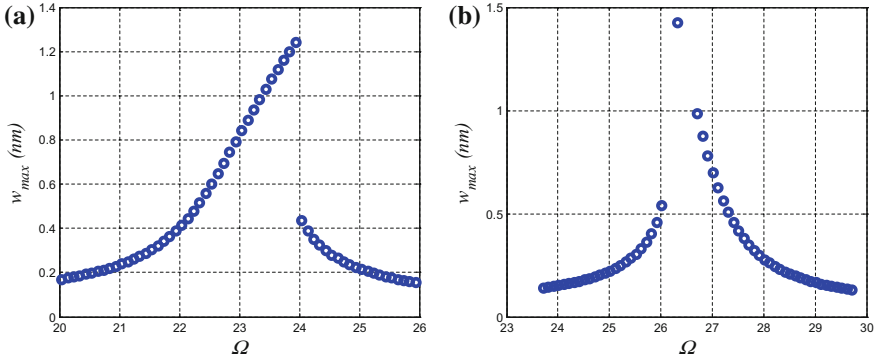
Fig. 5.49 Variation of the
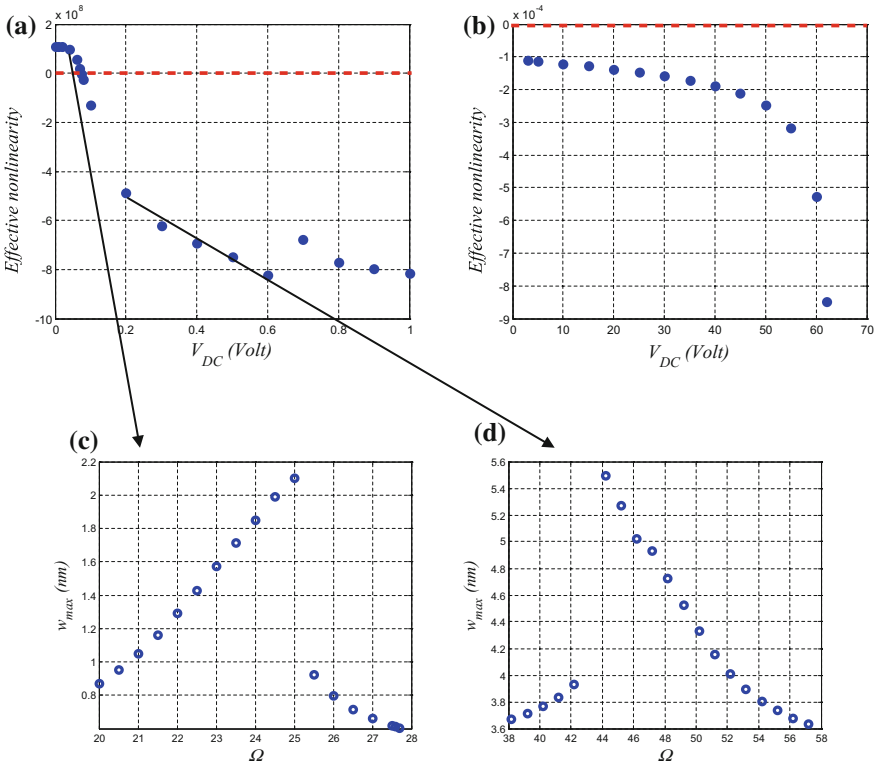effective nonlinearity of the
CNT with slack
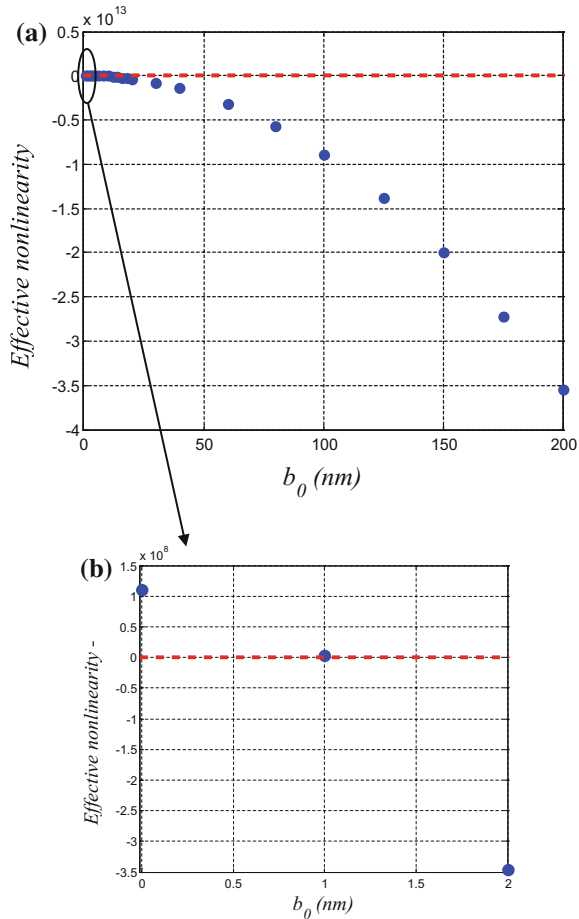
behavior. This means that for CNT with large aspect ratio, a tiny slack level will
soften the fundamental mode. To verify the results of Fig. 5.49, we integrate with
time the differential equations of motion to obtain the dynamic response of the slacked
CNT under small DC and AC harmonic load. Figures 5.50a, b show the response of a
0.5 nm and 1.5 nm slacked CNT, respectively, which verify the perturbation results.

The variation of the effective nonlinearity with the DC load for the unslaked CNT
case is shown in Fig. 5.51. In this case, the beam model applies up to $V_{DC} < 1$ Volt,
after which the string model is used. We can see from Fig. 5.51a, b that S is only
positive in this case in a very small range of DC load indicating a hardening behavior.
The results of the beam model were compared by those of the string model, in which
we can see that the CNT behavior is of softening type. Also the results are verified
using time integration of the equation of motion using the ROM, Fig. 5.51c, d.

Fig. 5.50 Frequency-response curves of (**a**) 0.5 nm and (**b**) 1.5 nm slacked CNT showing hardening and softening behaviors respectively. Results are shown for $V_{DC} = V_{AC} = 0.01$ Volt, and 100 quality factor

Fig. 5.51 Variation of the effective nonlinearity coefficient S of the unslacked CNT with the DC voltage while using (**a**) a beam model, and (**b**) a string model. Frequency-response curves of unslacked CNT for (**c**) $V_{DC} = 0.04$ Volt, and (d) $V_{DC} = 0.2$ Volt showing hardening and softening behaviors respectively. Results of Fig. 6.19c, d are shown for $V_{AC} = 0.01$ Volt, and 100 quality factor
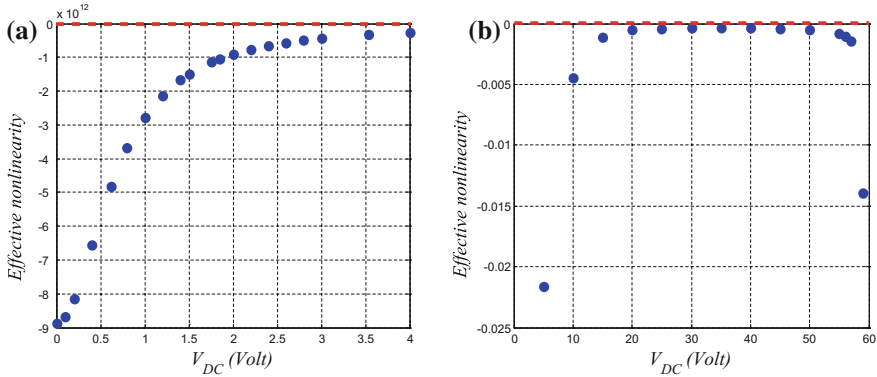
Fig. 5.52 Variation of the effective nonlinearity coefficient *S* of the 100 nm slacked CNT with the DC voltage while using (**a**) a beam model, and (**b**) a string model

Finally, the results of Fig. 5.51a, b are simulated for a 100 nm slacked CNT in Fig. 5.52a, b. Here also we notice that the beam model applies in the bending regime, i.e., $V_{DC} < 4$ Volt. Above this value, the string model is used. We can see also that we get the same behavior as the case of CNT with higher radius, Fig. 5.47. In this case, the CNT is locally dominated by a softening behavior due to the presence of the huge quadratic nonlinearity from the slack level. We notice also an increase of the effective nonlinearity, which is due to the presence of a source of cubic nonlinearity coming from the mid-plane stretching of the CNT. Finally, the effective nonlinearity starts to decrease near the pull-in zone where the electrostatic force starts to dominate the behavior of the slacked CNT.

References

1. Iijima, S. (1991). Helical microtubules of graphitic carbon. *Nature*, *354*, 56–58.
2. Craighead, H. G. (2000). Nanoelectromechanical systems. *Science*, *290*, 1532–1535.
3. Postma, H., Kozinsky, I., Husain, A., & Roukes, M. (2005). Dynamic range of nanotube- and nanowire-based electromechanical systems. *Applied Physics Letters*, *86*, 223105(1–3).
4. Sazonova, V., Yaish, Y., Üstünel, H., Roundy, D., Arias, T. A., & McEuen, P. L. (2004). A tunable carbon nanotubes electromechanical oscillator. *Nature*, *431*, 284–287.
5. Sazonova, V. A. (2006). A tunable carbon nanotube resonator, Ph.D. Thesis, Department of Physics, Cornell University.
6. Üstünel, H., Roundy, D., & Arias, T. A. (2005). Modeling a suspended nanotube oscillator. *Nano Letter*, *5*, 523–526.
7. Gibson, R. F., Ayorinde, E. O., & Wen, Y. F. (2007). Vibrations of carbon nanotubes and their composites: A review. *Composites Science and Technology*, *67*, 1–28.
8. Gao, R. P., Wang, Z. L., Bai, Z. G., de Heer, W. A., Dai, L. M., & Gao, M. (2000). Nanomechanics of individual carbon nanotubes from pyrolytically grown arrays. *Physical Review Letters*, *85*, 622–625.

9. Wang, Z. L., Gao, R. P., Poncharal, P., de Heer, W. A., Dai, Z. R., & Pan, Z. W. (2001). Mechanical and electrostatic properties of carbon nanotubes and nanowires. *Materials Science and Engineering C*, *16*, 3–10.

10. Dequesnes, M., Rotkin, S. V., & Aluru, N. R. (2002). Calculation of pull-in voltages for carbon-nanotube-based nanoelectromechanical switches. *Nanotechnology*, *13*, 120–131.

11. Sapmaz, S., Blanter, Y. M., Gurevich, L., & van der Zant, H. S. J. (2003). Carbon nanotubes as nanoelectromechanical systems. *Physical Review B*, *67*, 14–2354.

12. Dequesnes, M., Tang, S., & Aluru, N. R. (2004). Static and dynamic analysis of carbon nanotube-based switches. *Journal of Engineering Materials and Technology*, *126*, 230–237.

13. Lefèvre, R., Goffman, M. F., Derycke, V., Miko, C., Forró, L., Bourgoin, J. P., et al. (2005). Scaling law in carbon nanotube electromechanical devices. *Physical Review Letters*, *95*, 55–59.

14. Ke, C. H., & Espinosa, H. D. (2005). Numerical analysis of nanotube-based NEMS devices—Part I: Electrostatic charge distribution on multiwalled nanotubes. *Journal of Applied Mechanics*, *72*, 721–725.

15. Pugno, N., Ke, C. H., & Espinosa, H. D. (2005). Analysis of doubly clamped nanotube devices in the finite deformation regime. *Journal of Applied Mechanics*, *72*, 445–449.

16. Witkamp, B., Poot, M., & van der Zant, H. S. J. (2006). Bending-mode vibration of a suspended nanotube resonator. *Nano Letter*, *6*, 2904–2908.

17. Poot, M., Witkamp, B., Otte, M. A., & van der Zant, H. S. J. (2007). Modeling suspended carbon nanotube resonators. *Physica Status Solidus (b)*, *244*, 4252–4256.

18. Peng, H. B., Chang, C. W., Aloni, S., Yuzvinsky, T. D., & Zettl, A. (2007). Microwave electromechanical resonator consisting of clamped carbon nanotubes in an abacus arrangement. *Physical Review B*, *76*, 354–359.

19. Srivastava, D., & Barnard, S. T. (1997). Molecular dynamics simulation of large-scale carbon nanotubes on a shared-memory architecture. In *Proceedings of the 1997 ACM/IEEE Conference on Supercomputing*. San Jose, CA.

20. Sears, A. T. (2006). Carbon nanotube mechanics: continuum model development from molecular mechanics virtual experiments. Ph.D. Thesis, Virginia Polytechnic Institute and State University, Blacksburg, VA.

21. Hwang, H. J., & Lee, J. H. (2006). Molecular dynamics modeling of eectromechanical nanotube memory. *Journal of the Korean Physical Society*, *49*(3), 1136–1142.

22. Brodka, A., Kołoczek, J., Burian, A., Dore, J. C., Hannon, A. C., & Fonseca, A. (2006). Molecular dynamics simulation of carbon nanotube structure. *Journal of Molecular Structure*, *792–793*, 78–81.

23. Kang, J. W., Hwang, H. J., & Jiang, Q. (2006). A molecular dynamics study on oscillation of a carbon nanotube inside an encapsulating Boron-Nitride nanotube. *Journal of Computational and Theoretical Nanoscience*, *3*(6), 880–884(1–5).

24. Kang, J. W., Kang, D. Y., Choi, Y. G., Lee, S., & Hwang, H. J. (2009). Molecular dynamics study of tunable double-walled carbon nanotube oscillator. *Journal of Computational and Theoretical Nanoscience*, *6*(7), 1580–1584(1–5).

25. Kang, J. W., Won, C. S., Ryu, G. H., & Choi, Y. G. (2009). Molecular dynamics study on resonance characteristics of gigahertz carbon nanotube motor. *Journal of Computational and Theoretical Nanoscience*, *6*(1), 178–186(1–9).

26. Greaney, P. A., & Grossman, J. C. (2007). Nanomechanical energy transfer and resonance effects in single-walled carbon nanotubes. *Physical Review Letters*, *98*, 125503–125507.

27. Lu, J.-M., Wang, Y.-C., Chang, J.-G., Su, M.-H., & Hwang, C.-C. (2008). Molecular-dynamic investigation of buckling of double-walled carbon nanotubes under uniaxial compression. *Journal of the Physical Society of Japan*, *77*(4), 044603(1–7).

28. Shayan-Amin, S., Dalir, H., & Farshidianfar, A. (2009). Molecular dynamics simulation of double-walled carbon nanotube vibrations: comparison with continuum elastic theories. *Journal of Mechanics*, *25*(4).

29. Wang, X. Y., & Wang, X. (2004). Numerical simulation for bending modulus of carbon nanotubes and some explanations for experiment. *Composites Part B*, *35*, 79–86.

30. Lau, K. T., Chipara, M., Ling, H., & Hui, D. (2004). On the effective elastic moduli of carbon nanotubes for nanocomposite structures. *Composites Part B*, *35*, 95–101.
31. Garg, M. (2005). Mechanics of deformation of carbon nanotubes. MS thesis, Department of Mechanical Engineering, Massachuset Institute of Technology.
32. Yakobson, B., Brabec, C., & Bernholc, J. (1996). Nanomechanics of carbon tubes: instabilities beyond linear response. *Physical Review Letters*, *76*, 2511–2514.
33. Harik, V. M. (2002). Mechanics of carbon nanotubes: applicability of the continuum-beam models. *Computational Materials Science*, *24*, 328–342.
34. Harik, V. M. (2001). Ranges of applicability of the continuum beam model in the mechanics of carbon nanotubes and nanorods. *Solid State Communication*, *120*, 331–335.
35. Liu, J. Z., Zheng, Q., & Jiang, Q. (2001). Effect of a rippling mode on resonances of carbon nanotubes. *Physical Review Letters*, *86*, 43–46.
36. Pantano, A., Parks, D. M., & Boyce, M. C. (2004). Mechanics of deformation of single- and multi-wall carbon nanotubes. *Journal of the Mechanics and Physics of Solids*, *52*, 789–821.
37. Arroyo, M. (2004). Continuum mechanics and carbon nanotubes. In *Proceedings of the XXI ICTAM*. Warsaw, Poland.
38. Arroyo, M., & Belytschko, T. (2005). Continuum mechanics modeling and simulation of carbon nanotubes. *Meccanica*, *40*(4–6), 455–469.
39. Wang, L., Hu, H., & Guo, W. (2010). Thermal vibration of carbon nanotubes predicted by beam models and molecular dynamics. In *Proceedings of the Royal Society A, Mathematical, Physical, and Engineering Sciences*, rspa.2009.0609v1-rspa20090609.
40. Sears, A., & Batra, R. C. (2010). Carbon nanotube mechanics: molecular simulations and continuum models for carbon nanotubes. In *Virginia Space Grant Consortium 2010 Student Research Conference, Department of Engineering Science and Mechanics: Virginia Polytechnic Institute and State University Blacksburg*.
41. Conley, W. G., Raman, A., Krousgrill, C. M., & Mohammadi, S. (2008). Nonlinear and nonplanar dynamics of suspended nanotube and nanowire resonators. *Nano Letters*, *8*, 1590–1595.
42. Elishakoff, I., & Pentaras, D. (2009). Fundamental natural frequencies of double-walled carbon nanotubes. *Journal of Sound and Vibration*, *322*, 652–664.
43. Elishakoff, I., & Pentaras, D. (2009). Natural frequencies of carbon nanotubes based on simplified Bresse-Timoshenko theory. *Journal of Computational and Theoritical Nanoscience*, *6*, 1527–1531.
44. Georgantzinos, S. K., Giannopoulos, G. I., & Anifantis, N. K. (2009). An efficient numerical model for vibration analysis of single-walled carbon nanotubes. *Journal of Computational Mechanics*, *43*, 731–741.
45. Hawwa, M. A., & Al-Qahtani, H. M. (2010). Nonlinear oscillations of a double-walled carbon nanotube. *Computational Material Science*, *48*, 140–143.
46. Ke, C. H., & Espinosa, H. D. (2006). In situ electron microscopy electromechanical characterization of a bistable NEMS device. *Small*, *2*(12), 1484–1489.
47. Ke, C. H., Espinosa, H. D., & Pugno, N. (2005). Numerical analysis of nanotube-based NEMS devices—Part II: Role of finite kinematics, stretching and charge concentrations. *Journal of Applied Mechanics*, *72*, 726–731.
48. Ke, C. H., Pugno, N., Peng, B., & Espinosa, H. D. (2005). Experiments and modeling of carbon nanotube-based NEMS devices. *Journal of the Mechanics and Physics of solids*, *53*, 1314–1333.
49. Isacsson, A., Kinaret, J. M., & Kaunisto, R. (2007) Nonlinear resonance in a three-terminal carbon nanotube resonator. *Nanotechnology*, *18*, 95203(1–8).
50. Isacsson, A., & Kinaret, J. M. (2009) Parametric resonances in electrostatically interacting carbon nanotube arrays. *Physical Review B*, *79*, 165418(1–11).
51. Krishnan, A., Dujardin, E., Ebbesen, T. W., Yianilos, P. N., & Treacy, M. M. J. (1998). Young's modulus of single-walled nanotubes. *Physical Review B*, *58*, 14013–14019.
52. Kim, P., & Lieber, C. M. (1999). Nanotube nanotweezers. *Science Magazine*, *286*(5447), 2148–2150.

53. Poncharal, P., Wang, Z. L., Ugarte, D., & de Heer, W. A. (1999). Electrostatic deflections and electromechanical resonances of carbon nanotubes. *Science*, *283*, 1513–1516.

54. Babic, B., Furer, J., Sahoo, S., Farhangfar, S., & Schonenberger, C. (2003). Intrinsic thermal vibrations of suspended doubly clamped single-wall carbon nanotubes. *Nano Letters*, *3*, 1577–1580.

55. Dujardin, E., Derycke, V., Goffman, M. F., Lefèvre, R., & Bourgoin, J. P. (2005). Self-assembled switches based on electroactuated multiwalled nanotubes. *Applied Physics Letters*, *87*, 1931–1938.

56. Rabieirad, L., Kim, S., Shim, M., & Mohammadi, S. (2005). Doubly clamped single-walled carbon nanotube resonators operating in MHz frequencies. In *Proceedings of 2005 5th IEEE Conference on Nanotechnology*. Nagoya, Japan.

57. Bak, J. H., Kim, Y. D., Hong, S. S., Lee, B. Y., Lee, S. R., Jang, J. H., et al. (2008). High-frequency micromechanical resonators from aluminium-carbon nanotube nanolaminates. *Nature Materials*, *7*, 459–463.

58. San Paulo, A., Black, J, García-Sanchez, D., Esplandiu, M. J., Aguasca, A., Bokor, J., F. Perez-Murano, F., & Bachtold, A. (2008). Mechanical detection and mode shape imaging of vibrational modes of micro and nanomechanical resonators by dynamic force microscopy. *Journal of Physics: Conference Series*, *100*, 052009(1–5).

59. Amlani, I., Lee, K. F., Deng, J., & Wong, H. S. P. (2009). Measuring frequency response of a single-walled carbon nanotube common-sourcea. *IEEE Transactions on Nanotechnology*, *8*, 226–233.

60. Ren, L., Pint, C. L., Booshehri, L. G., Rice, W. D., Wang, X., Hilton, D. J., et al. (2009). Carbon nanotube terahertz polarizer. *Nano Letters*, *9*, 2610–2613.

61. Kienle, D., & Léonard, F. (2000). Terahertz response of carbon nanotube transistors. *Physical Review Letters*, *103*, 026601(1–4).

62. Lu, R. F., Lu, Y. P., Lee, S. Y., Ha, K. L., & Deng, W. Q. (2009). Terahertz response in single-walled carbon nanotube transistor: A real-time quantum dynamics simulation. *Nanotechnology*, *20*, 505401(1–4).

63. Kang, J. W., Lee, J. H., Lee, H. J., & Hwang, H. J. (2005). A study on carbon nanotube bridge as a electromechanical memory device. *Physica E*, *27*, 332–340.

64. Garcia-Sanchez, D., San Paulo, A., Esplandiu, M. J., Perez-Murano, F., Forrò, L., Aguasca, A., & Bachtold, A. (2007). Mechanical detection of carbon nanotube resonator vibrations. *Physical Review Letters*, *99*, 085501(1–4).

65. Mayoof, F. N., & Hawwa, M. A. (2009). Chaotic behavior of a curved carbon nanotube under harmonic excitation. *Journal of Chaos, Solitons & Fractals*, *42*, 1860–1867.

66. Meirovitch, L. (2001). *Fundamentals of vibrations*. New York: McGraw Hill.

67. Rao, S. S. (2004). *Mechanical vibrations* (4th ed.). New Jersey: Prentice Hall.

68. Dawe, D. J. (1971). The Ttransverse vibartion of shallow arches using the displacement method. *International Journal of Mechanical Sciences*, Pergamon Press, *13*, 713–720.

69. Nayfeh, A. H. (2000). *Nonlinear interactions*. New-York, United-States: Wiley Interscience.

70. Itô, K. (Ed.). (1993). Methods other than difference methods. *§303I in encyclopedic dictionary of mathematics* (2nd ed.) (vol. 2, pp. 1139–1980). Cambridge, MA: MIT Press.

71. Ouakad, H. M. (2013). The response of a micro-electro-mechanical system (MEMS) cantilever-paddle gas sensor to mechanical shock loads. *Journal of Vibration and Control*, in press. doi:10.1177/1077546313514763.

72. Younis, M. I., Abdel-Rahman, E. M., & Nayfeh, A. H. (2003). A Reduced-order model for electrically actuated microbeam-based MEMS. *Journal of Microelectromechanical Systems*, *12*, 672–680.

73. Reddy, J. N. (2002). *Energy principles and variational methods in applied mechanics*. New York: Wiley and Sons.

74. Hayt, W. H., & Buck, J. A. (2001). *Engineering electromagnetics*. New York, United-States: McGraw-Hill.

75. Nathanson, H. C., & Wickstrom, R. A. (1965). A resonant gate silicon surface transistor with high Q bandpass properties. *IEEE Applied Physics Letters*, *7*, 84–86.

76. Nathanson, H. C., Newell, W. E., Wickstrom, R. A., & Davis, J. R. (1967). The Resonant gate transistor. *IEEE Transactions on Electron Devices*, *14*, 117–133.

77. Newell, W. (1968). Miniaturization of tuning forks. *Science*, *161*(3848), 1320–1326.

78. Abdel-Rahman, E. M., Younis, M. I., & Nayfeh, A. H. (2002). Characterization of the mechanical behavior of an electrically actuated microbeam. *Journal of Micromechanics and Microengineering*, *12*, 759–766.

79. Younis, M. I., & Nayfeh, A. H. (2003). A study of the nonlinear response of a resonant microbeam to an electric actuation. *Nonlinear Dynamics*, *31*, 91–117.

80. Nayfeh, A. H., & Younis, M. I. (2005). Dynamics of MEMS resonators under superharmonic and subharmonic excitations. *Journal of Micromechanics and Microengineering*, *15*, 1840–1847.

81. Nayfeh, A. H., Younis, M. I., & Abdel-Rahman, E. M. (2005). Reduced-order models for MEMS applications. *Nonlinear Dynamics*, *41*, 211–236.

82. Krylov, S., & Maimon, R. (2004). Pull-in dynamics of an elastic beam actuated by continuously distributed electrostatic force. *Journal of Vibration and Acoustics*, *126*, 332–342.

83. Elata, D., & Bamberger, H. (2006). On the dynamic pull-in of electrostatic actuators with multiple degrees of freedom and multiple voltage sources. *Journal of Microelectromechanical Systems*, *15*, 131–140.

84. Nayfeh, A. H., Younis, M. I., & Abdel-Rahman, E. M. (2007). Dynamic pull-in phenomenon in MEMS resonators. *Nonlinear Dynamics*, *48*, 153–163.

85. Thompson, J. M. T., & Stewart, H. B. (2001). *Nonlinear dynamics and chaos*. New York, United-States: Wiley.

86. Alsaleem, F. M., Younis, M. I., & Ouakad, H. M. (2009). On the nonlinear resonances and dynamic pull-in of electrostatically actuated resonators. *Journal of Micromechanics and Microengineering*, *19*(4), 045013.

87. Wolfram, S. (2000). *The Mathematica Book* (Vol. 100, pp. 7237–61820). New York, NY, USA: Cambridge University Press and Wolfram Research Inc.

88. Noor, A. K., & Nemeth, M. P. (1980). Micropolar beam models for lattice grids with rigid joints. *Computer Methods in Applied Mechanics and Engineering*, *21*(2), 249–263.

89. Harris, P. J. F. (1999). *Carbon nanotubes and related structures*. Cambridge, MA, United-States: Cambridge University Press.

90. Yu, M. F. (2004). Fundamental mechanical properties of carbon nanotubes: current understanding and the related experimental studies. *Journal of Engineering Materials and Technology*, *126*, 271–278.

91. Akita, S., Nakayama, Y., Mizooka, S., Takano, Y., Okawa, T., Miyatake, Y., et al. (2001). Nanotweezers consisting of carbon nanotubes operating in an atomic force microscope. *Applied Physics Letters*, *79*(11), 1691–1694.

92. Ouakad, H. M., & Younis, M. I. (2010). The dynamic behavior of MEMS arch resonators actuated electrically. *International Journal of Non-Linear Mechanics*, *45*(7), 704–713.

93. Ouakad, H. M. (2014). Static response and natural frequencies of microbeams actuated by out-of-plane electrostatic fringing-fields. *International Journal of Non-Linear Mechanics*, *63*, 39–48.

94. Abdel-Rahman, E. M., Emam, S. A., & Nayfeh, A. H. (2003). A generalized model of electrically actuated microbeam-based MEMS devices. In *Proceedings of the DETC.03 ASME 2003 Design Engineering Technical Conference and Computers and Information in Engineering Conference*. Chicago, Illinois, USA.

95. Nayfeh, A. H., & Pai, P. F. (2004). *Linear and nonlinear structural mechanics*. New York, United-States: Wiley.

96. Nayfeh, A. H., & Balachandran, B. (1995). *Applied nonlinear dynamics*. New York: Wiley.

97. Kuttler, J. R., & Sigillito, V. G. (1981). On curve veering. *Journal of Sound and Vibration*, *75*, 585–588.

98. Perkins, N. C., & Mote, C. D, Jr. (1986). Comments on curve veering in eigenvalue problems. *Journal of Sound and Vibration*, *106*, 451–463.

99. Arafat, H. N., & Nayfeh, A. H. (2003). Non-linear responses of suspended cables to primary resonance excitations. *Journal of Sound and Vibration*, *266*, 325–354.
100. Rega, G. (2004). Nonlinear vibrations of suspended cables-Part I: Modeling and analysis. *Journal of Applied Mechanics Review*, *57*, 443–478.
101. Lin, J., & Parker, R. G. (2001). Natural frequency veering in planetary gears. *Mechanics of Structures and Machines*, *29*, 411–429.
102. Nayfeh, A. H. (1981). *Introduction to perturbation techniques*. New York, United-States: Wiley Interscience.